

<sub>1</sub> A novel inf–sup–based volumetric constraint ratio and  
<sub>2</sub> its implementation via mixed FE-meshfree formulation

<sub>3</sub> Junchao Wu<sup>a,\*</sup>, Yingjie Chu<sup>b</sup>, Yangtao Xu<sup>a</sup>

<sup>a</sup> Key Laboratory for Intelligent Infrastructure and Monitoring of Fujian Province, College  
of Civil Engineering, Huaqiao University , Xiamen, Fujian, 361021, China

<sup>b</sup> Fujian Key Laboratory of Digital Simulations for Coastal Civil Engineering, Department  
of Civil Engineering, Xiamen University , Xiamen, Fujian, 361005, China

---

<sub>4</sub> **Abstract**

Numerical formulations for incompressible materials often suffer from volumetric locking, which reduces the accuracy of displacement solutions and introduces oscillations in the pressure field. A well-chosen constraint ratio can mitigate this issue, but traditional approaches lack a theoretical foundation based on the inf–sup (or LBB) condition, which is essential for the stability of mixed formulations. This paper introduces a novel optimal constraint ratio derived from the inf–sup condition to address volumetric locking. The inf–sup test, a numerical tool for verifying the inf–sup condition, is reaffirmed to be equivalent to the inf–sup condition through a variational approach. By incorporating a complete polynomial space whose dimension matches the number of displacement degrees of freedom (DOFs), a new inf–sup value estimator is developed, explicitly considering the constraint ratio. For a given number of displacement DOFs, when the pressure DOFs of a numerical formulation remain below a stabilized number that falls into the optimal constraint ratio range, this numerical formulation actually satisfies the inf–sup condition. To implement the optimal constraint ratio, a mixed finite element and meshfree formulation is proposed, where displacements are discretized using traditional finite element approximations, and pressures are approximated via the reproducing kernel meshfree method. Leveraging the globally smooth reproducing kernel shape functions, the constraint ratio can be flexibly adjusted to meet the inf–sup condition without the limit of element. For computational efficiency and ease of implementation, pressure nodes are placed on selected displacement nodes to maintain the optimal constraint ratio. Inf–sup tests and a series of 2D and 3D incompressible elasticity examples validate the proposed constraint ratio, demonstrating its effectiveness in eliminating volumetric locking and enhancing the performance of mixed finite element and meshfree formulations.

<sub>5</sub> **Keywords:** Optimal constraint ratio, Inf–sup condition estimator, Volumetric  
<sub>6</sub> locking, Mixed formulation, Reproducing kernel meshfree approximation

---

---

\*Corresponding author

Email address: [jcwu@hqu.edu.cn](mailto:jcwu@hqu.edu.cn) (Junchao Wu)

7      **1. Introduction**

8      The volumetric constraint is a necessary condition in the numerical formulation  
 9      of incompressible materials like rubber and hydrogel. Proper imposition of  
 10     this constraint is crucial for obtaining better numerical solutions; insufficient or  
 11     excessive constraints will reduce the accuracy and stability of the solution [1].  
 12     The volumetric constraint ratio [2], denoted as  $r$ , is often used to measure the  
 13     level of constraint. It is defined as the total degrees of freedom (DOFs) of dis-  
 14     placement divided by the total DOFs of pressure. Ideally, the optimal constraint  
 15     ratio should be consistent with its governing partial differential equations. For  
 16     example, in the two-dimensional (2D) case, the optimal constraint ratio is 2,  
 17     since there are two governing equations for displacement and one for pressure.  
 18     When the constraint ratio is less than 2, the formulation suffers from volumetric  
 19     locking, while a constraint ratio greater than 2 can cause a coarse solution for  
 20     pressure. These observations have been summarized as follows[2]:

$$r = \frac{2n_u}{n_p}, \quad \begin{cases} r > 2 & \text{too few constraints} \\ r = 2 & \text{optimal} \\ r < 2 & \text{too many constraints} \\ r \leq 1 & \text{severe locking} \end{cases} \quad (1)$$

21     where  $n_u$  and  $n_p$  are the numbers of control nodes for displacement and pressure,  
 22     respectively. Classifying the locked status via the constraint ratio is straight-  
 23     forward but imprecise. For instance, the constraint ratio can remain 2 while  
 24     the pressure is discretized using continuous shape functions identical to the  
 25     displacement's approximation. However, volumetric locking still exists in this  
 26     formulation [2].

27     The inf-sup condition, also known as the Ladyzhenskay–Babuka–Brezzi  
 28     (LBB) condition [3, 4], is a more precise requirement for a locking-free for-  
 29     mulation. This condition is based on the mixed formulation framework, and  
 30     when the inf-sup condition is satisfied, both the accuracy and stability of the  
 31     mixed-formulation can be ensured. However, verifying the inf-sup condition is  
 32     non-trivial. An eigenvalue problem namely inf-sup test can be used to check  
 33     this condition numerically [5, 6, 7, 8]. Analytically, Brezzi and Fortin proposed  
 34     a two-level projection framework that always satisfies the inf-sup condition, al-  
 35     lowing it to be checked by identifying whether the formulation is included in  
 36     this framework. Both analytical and numerical methods to check the inf-sup  
 37     condition are complex, and the relationship between the constraint ratio and  
 38     the inf-sup condition remains unclear.

39     To address volumetric constraint issues, adjusting the constraint ratio to an  
 40     appropriate level is commonly used and easily implemented. In traditional finite  
 41     element methods (FEM), this adjustment is carried out based on elements since  
 42     the DOFs are embedded in each element. Conventional FEM often exhibits  
 43     an over-constrained status. Reducing the approximation order of pressure in  
 44     mixed formulation can alleviate the constraint burden, such as with the well-  
 45     known Q4P1 (4-node quadrilateral displacement element with 1-node piecewise

constant pressure element) and Q8P3. Globally, using continuous shape functions to link the local pressure DOFs in each element can also reduce the total number of pressure DOFs and increase the constraint ratio, such as with T6C3 (6-node triangular displacement element with 3-node continuous linear pressure element) and Q9C4 (Taylor–Hood element) [9]. These schemes belong to the mixed formulation framework and can also be implemented through a projection approach, where the pressure approximant is projected into a lower-dimensional space. Examples include selective integration methods [10, 11], B–bar or F–bar methods [12, 13, 14, 15], pressure projection methods [16, 17, 18, 19, 20], and enhanced strain method [21]. Meanwhile, conventional 3-node triangular elements arranged in a regular cross pattern can also reduce the dimension of the pressure space [22]. It should be noted that not all of these methods meet the inf–sup condition despite alleviating volumetric locking and producing a good displacement solution. Some methods, like Q4P1, show significant oscillation for the pressure solution, known as spurious pressure mode or checkerboard mode [22]. In such cases, additional stabilization approaches, such as variational multi-scale stabilization (VMS) [23, 24, 25, 26, 27], Galerkin/least-squares (GLS) [28], or Streamline upwind/Petrov–Galerkin formulation (SUPG) [29, 30] are required to eliminate the oscillations in pressure.

Another class of FEM methods adjusts the constraint ratio by increasing the displacement DOFs. For instance, based on 3-node triangular elements, Arnold et al. [31, 32] used a cubic bubble function in each element to increase the displacement DOFs, known as the MINI element. It has been shown that this method belongs to the VMS framework [33], and its fulfillment of the inf–sup condition can be analytically evidenced using the two-level projection framework [7]. The Crouzeix–Raviart element [34] transfers the DOFs from the triangular vertices to edges, increasing the constraint ratio since, for triangular topology, the number of edges is greater than that of vertices. More details about FEM technology for volumetric constraint issues can be found in Refs. [2, 4, 35].

In the past two decades, various novel approximations equipped with globally smooth shape functions, such as moving least-squares approximation [36], reproducing kernel approximation [37, 38], radial basis functions [39, 40], maximum-entropy approximation [41], and NURBS approximation [42, 43], have been proposed. In these approaches, the approximant pressure evaluated by the derivatives of globally continuous shape functions also maintains a constraint ratio of 2 in 2D incompressible elasticity problems. However, the corresponding results still show lower accuracy caused by locking [44, 45]. Widely-used locking-free technologies for FEM are introduced in these approaches to enhance their performance. For example, Moutsanidis et al. [46, 47] employed selective integration and B–bar, F–bar methods for reproducing kernel particle methods. Wang et al. [48] applied selective integration schemes with bubble-stabilized functions to node-based smoothed particle FEM. Elguedj et al. [49] proposed the B–bar and F–bar NURBS formulations for linear and nonlinear incompressible elasticity. Chen et al. [50] adopted the pressure projection approach for reproducing kernel formulations for nearly-incompressible problems, which was later extended

to Stokes flow formulations by Goh et al. [51]. Bombarde et al. [52] developed a block-wise NURBS formulation for shell structures, eliminating locking via pressure projection. Casquero and Golestanian [53] proposed a NURBS-based continuous-assumed-strain element to alleviate volumetric locking. Most of these approximations offer better flexibility for arranging DOFs since their shape function constructions are no longer element-dependent. Huerta et al.[54] proposed a reproducing kernel approximation with divergence-free basis functions to avoid volumetric strain entirely , although this approach is unsuitable for compressible cases. Wu et al. [55] added extra displacement DOFs in FEM elements to resolve the locking issue, constructing local shape functions using generalized meshfree interpolation to maintain consistency. Vu-Huu et al. [56] employed different-order polygonal finite element shape functions to approximate displacement and pressure, embedding a bubble function in each element for stabilization.

This work proposes a more precise optimal volumetric constraint ratio and implements a locking-free mixed FE-meshfree formulation with this optimal constraint ratio. Firstly, the inf-sup condition is derived in a new form, showing that the inf-sup value equals to the lowest non-zero eigenvalue of dilatation stiffness in the context of variational analysis. Subsequently, involving a complete polynomial space with dimensions identical to displacement DOFs, the number of non-zero eigenvalues can be analytically calculated, and a new estimator considering the constraint ratio is established. From this estimator, the optimal constraint ratio is defined with a stabilized number of pressure nodes. If the constraint ratio exceeds the locking ratio, the formulation will show severe locking. When the constraint ratio is lower than the optimal ratio, the formulation achieves satisfactory results, and the inf-sup condition is fulfilled. This estimator provides a strong link between the inf-sup value and the pressure DOFs, making it possible to justify the locking status by counting the pressure nodes. Furthermore, a mixed FE-meshfree formulation is proposed to verify the optimal constraint ratio. In this mixed formulation, the displacement is approximated by traditional finite element methods, and the pressure is discretized by reproducing kernel meshfree approximation. With the aid of global RK shape functions, the pressure's DOFs can be adjusted arbitrarily without considering approximation order and numerical integration issues to maintaining the constraint ratio as optimal.

The remainder of this paper is organized as follows: Section 2 reviews the mixed formulation framework for incompressible elasticity problems. In Section 3, a novel estimator of the inf-sup value is developed, from which the optimal constraint ratio is obtained. Section 4 introduces the mixed FE-meshfree formulation and its corresponding nodal distribution schemes. Section 5 verifies the proposed optimal constraint ratio using a set of benchmark incompressible elasticity examples, studying error convergence and stability property for the mixed FE-meshfree approximation. Finally, the conclusions are presented in Section 6.

<sup>136</sup> **2. Mixed-formulation**

<sup>137</sup> *2.1. Nearly-incompressible elasticity*

<sup>138</sup> Consider a body  $\Omega \in \mathbb{R}^{n_d}$  with boundary  $\Gamma$  in  $n_d$ -dimension, where  $\Gamma_t$  and  
<sup>139</sup>  $\Gamma_g$  denote its natural boundary and essential boundary, respectively, such that  
<sup>140</sup>  $\Gamma_t \cup \Gamma_g = \Gamma$ ,  $\Gamma_t \cap \Gamma_g = \emptyset$ . The corresponding governing equations for the mixed  
<sup>141</sup> formulation are given by:

$$\begin{cases} \nabla \cdot \boldsymbol{\sigma} + \mathbf{b} = \mathbf{0} & \text{in } \Omega \\ \frac{p}{\kappa} + \nabla \cdot \mathbf{u} = 0 & \text{in } \Omega \\ \boldsymbol{\sigma} \cdot \mathbf{n} = \mathbf{t} & \text{on } \Gamma_t \\ \mathbf{u} = \mathbf{g} & \text{on } \Gamma_g \end{cases} \quad (2)$$

<sup>142</sup> where  $\mathbf{b}$  denotes the prescribed body force in  $\Omega$ .  $\mathbf{t}, \mathbf{g}$  are prescribed traction and  
<sup>143</sup> displacement on natural and essential boundaries, respectively.  $\mathbf{u}$  and  $p$ , standing  
<sup>144</sup> for displacement and hydrostatic pressure, respectively, are the variables of  
<sup>145</sup> this problem.  $\nabla$  is the gradient tensor defined by  $\nabla = \frac{\partial}{\partial x_i} \mathbf{e}_i$ .  $\boldsymbol{\sigma}$  denotes the  
<sup>146</sup> stress tensor and has the following form:

$$\boldsymbol{\sigma}(\mathbf{u}, p) = p \mathbf{1} + 2\mu \nabla^d \mathbf{u} \quad (3)$$

<sup>147</sup> in which  $\mathbf{1} = \delta_{ij} \mathbf{e}_i \otimes \mathbf{e}_j$  is the second-order identity tensor.  $\nabla^d \mathbf{u}$  is the deviatoric  
<sup>148</sup> gradient of  $\mathbf{u}$  and can be evaluated by:

$$\nabla^d \mathbf{u} = \frac{1}{2} (\mathbf{u} \nabla + \nabla \mathbf{u}) - \left( \frac{1}{3} \nabla \cdot \mathbf{u} \right) \mathbf{1} \quad (4)$$

<sup>149</sup> and  $\kappa, \mu$  are the bulk modulus and shear modulus, respectively, and they can  
<sup>150</sup> be represented by Young's modulus  $E$  and Poisson's ratio  $\nu$ :

$$\kappa = \frac{E}{2(1-2\nu)}, \quad \mu = \frac{E}{3(1+\nu)} \quad (5)$$

<sup>151</sup> In accordance with the Galerkin formulation, the weak form can be given  
<sup>152</sup> by: Find  $\mathbf{u} \in V, p \in Q$ , such that

$$\begin{cases} a(\mathbf{v}, \mathbf{u}) + b(\mathbf{v}, p) = f(\mathbf{v}) & \forall \mathbf{v} \in V \\ b(\mathbf{u}, q) + c(q, p) = 0 & \forall q \in Q \end{cases} \quad (6)$$

<sup>153</sup> with the spaces  $V, Q$  defined by:

$$V = \{\mathbf{v} \in H^1(\Omega)^2 \mid \mathbf{v} = \mathbf{g}, \text{ on } \Gamma_g\} \quad (7)$$

$$Q = \{q \in L^2(\Omega) \mid \int_{\Omega} q d\Omega = 0\} \quad (8)$$

<sup>154</sup> where  $a : V \times V \rightarrow \mathbb{R}$ ,  $b : V \times Q \rightarrow \mathbb{R}$  and  $c : Q \times Q \rightarrow \mathbb{R}$  are bilinear forms,  
<sup>155</sup> and  $f : V \rightarrow \mathbb{R}$  is the linear form. In elasticity problems, they are given by:

$$a(\mathbf{v}, \mathbf{u}) = \int_{\Omega} \nabla^d \mathbf{v} : \nabla^d \mathbf{u} d\Omega \quad (9)$$

$$b(\mathbf{v}, q) = \int_{\Omega} \nabla \cdot \mathbf{v} q d\Omega \quad (10)$$

$$c(q, p) = - \int_{\Omega} \frac{1}{3\kappa} q p d\Omega \quad (11)$$

$$f(\mathbf{v}) = \int_{\Gamma_t} \mathbf{v} \cdot \mathbf{t} d\Gamma + \int_{\Omega} \mathbf{v} \cdot \mathbf{b} d\Omega \quad (12)$$

<sup>156</sup> 2.2. Ritz–Galerkin problem and volumetric locking

<sup>157</sup> In the mixed-formulation framework, the displacement and pressure can be  
<sup>158</sup> discretized by different approximations. The approximant displacement  $\mathbf{u}_h$  and  
<sup>159</sup> approximant pressure  $p_h$  can be expressed by:

$$\mathbf{u}_h(\mathbf{x}) = \sum_{I=1}^{n_u} N_I(\mathbf{x}) \mathbf{u}_I, \quad p_h(\mathbf{x}) = \sum_{K=1}^{n_p} \Psi_K(\mathbf{x}) p_K \quad (13)$$

<sup>160</sup> where  $N_I$  and  $\Psi_K$  are the shape functions for the displacement and pressure,  $\mathbf{u}_I$   
<sup>161</sup> and  $p_K$  are the corresponding coefficients. Leading these approximations into  
<sup>162</sup> the weak form of Eq. (6) yields the following Ritz–Galerkin problems: Find  
<sup>163</sup>  $\mathbf{u}_h \in V_h$ ,  $p_h \in Q_h$ , such that

$$\begin{cases} a(\mathbf{v}_h, \mathbf{u}_h) + b(\mathbf{v}_h, p_h) = f(\mathbf{v}_h) & \forall \mathbf{v}_h \in V_h \\ b(\mathbf{u}_h, q_h) + c(q_h, p_h) = 0 & \forall q_h \in Q_h \end{cases} \quad (14)$$

<sup>164</sup> where the spaces  $V_h \subseteq V$ ,  $Q_h \subseteq Q$  are defined by:

$$V_h = \{\mathbf{v}_h \in (\text{span}\{N_I\}_{I=1}^{n_u})^{n_d} | \mathbf{v}_h = \mathbf{g}, \text{ on } \Gamma_g\} \quad (15)$$

$$Q_h = \{q_h \in \text{span}\{\Psi_K\}_{K=1}^{n_p} | \int_{\Omega} q_h d\Omega = 0\} \quad (16)$$

<sup>165</sup> For nearly incompressible material, the Poisson ratio approaches 0.5, and  
<sup>166</sup> the bulk modulus  $\kappa$  will tend to infinity based on Eq. (5). Then, the bilinear  
<sup>167</sup> form  $c$  in Eq. (11) tends to zero. And the weak form of Eq. (14) becomes an  
<sup>168</sup> enforcement of the volumetric strain  $\nabla \cdot \mathbf{u}_h$  to be zero using the Lagrangian  
<sup>169</sup> multiplier method, where  $p_h$  is the Lagrangian multiplier.

<sup>170</sup> Furthermore, from the second line of Eq. (14), we have:

$$b(\mathbf{u}_h, q_h) + c(q_h, p_h) = (q_h, \nabla \cdot \mathbf{u}_h) - (q_h, \frac{1}{3\kappa} p_h) = 0, \quad \forall q_h \in Q_h \quad (17)$$

<sup>171</sup> or

$$(q_h, 3\kappa \nabla \cdot \mathbf{u}_h - p_h) = 0, \quad \forall q_h \in Q_h \quad (18)$$

<sup>172</sup> where  $(\bullet, \bullet)$  is the inner product operator evaluated by:

$$(q, p) := \int_{\Omega} q p d\Omega \quad (19)$$

<sup>173</sup> Obviously, in Eq. (18),  $p_h$  is the orthogonal projection of  $3\kappa \nabla \cdot \mathbf{u}_h$  with respect  
<sup>174</sup> to the space  $Q_h$  [1], and, for further development, we use the nabla notation  
<sup>175</sup> with an upper tilde to denote the projection operator, i.e.,  $p_h = \tilde{\nabla} \cdot \mathbf{u}_h$ . In this  
<sup>176</sup> circumstance, the bilinear form  $b$  in the first line of Eq. (14) becomes:

$$\begin{aligned} b(\mathbf{v}_h, p_h) &= (\underbrace{\nabla \cdot \mathbf{v}_h - \tilde{\nabla} \cdot \mathbf{v}_h, p_h}_0) + (\tilde{\nabla} \cdot \mathbf{v}_h, \underbrace{p_h}_{3\kappa \tilde{\nabla} \cdot \mathbf{u}_h}) \\ &= (\tilde{\nabla} \cdot \mathbf{v}_h, 3\kappa \tilde{\nabla} \cdot \mathbf{u}_h) \\ &= \tilde{a}(\mathbf{v}_h, \mathbf{u}_h) \end{aligned} \quad (20)$$

<sup>177</sup> where the bilinear form  $\tilde{a} : V_h \times V_h \rightarrow \mathbb{R}$  is defined by:

$$\tilde{a}(\mathbf{v}_h, \mathbf{u}_h) = \int_{\Omega} 3\kappa \tilde{\nabla} \cdot \mathbf{v}_h \tilde{\nabla} \cdot \mathbf{u}_h d\Omega \quad (21)$$

<sup>178</sup> Accordingly, the problem of Eq. (14) becomes a one-variable form: Find  
<sup>179</sup>  $\mathbf{u}_h \in V_h$ , such that

$$a(\mathbf{v}_h, \mathbf{u}_h) + \tilde{a}(\mathbf{v}_h, \mathbf{u}_h) = f(\mathbf{v}_h), \quad \forall \mathbf{v}_h \in V_h \quad (22)$$

<sup>180</sup> As  $\kappa \rightarrow \infty$ , Eq. (22) can be regarded as an enforcement of volumetric strain  
<sup>181</sup> using the penalty method, where  $\tilde{a}$  is the penalty term. However, it should  
<sup>182</sup> be noted that, if the mixed-formulation wants to obtain a satisfactory result,  
<sup>183</sup> this orthogonal projection must be surjective [57]. In the case where it is not  
<sup>184</sup> surjective, for a given  $p_h \in Q_h$ , it may not be possible to find a  $\mathbf{u}_h \in V_h$  such that  
<sup>185</sup>  $p_h = 3\kappa \nabla \cdot \mathbf{u}_h$ . This will lead to a much smaller displacement than expected and  
<sup>186</sup> an oscillated pressure result. This phenomenon is called volumetric locking.

### <sup>187</sup> 3. Optimal volumetric constraint ratio

#### <sup>188</sup> 3.1. Inf-sup condition and its eigenvalue problem

<sup>189</sup> To ensure the surjectivity of orthogonal projection and satisfactory results,  
<sup>190</sup> the approximations of Eq.(7) should satisfy the inf-sup condition, also known  
<sup>191</sup> as the Ladyzhenskaya–Babuška–Brezzi condition [4]:

$$\inf_{q_h \in Q_h} \sup_{\mathbf{v}_h \in V_h} \frac{|b(q_h, \mathbf{v}_h)|}{\|q_h\|_Q \|\mathbf{v}_h\|_V} \geq \beta > 0 \quad (23)$$

<sup>192</sup> in which  $\beta$ , namely the inf-sup value, is a constant independent of the char-  
<sup>193</sup> acterized element size  $h$ . The Appendix A lists the displacement and pressure

<sup>194</sup> error estimators for mixed-formulations. These estimators imply how the inf-  
<sup>195</sup> sup value  $\beta$  affects solution's accuracy. The norms  $\|\bullet\|_V$  and  $\|\bullet\|_Q$  can be  
<sup>196</sup> flexibly defined by:

$$\|\mathbf{v}\|_V^2 := \int_{\Omega} \nabla^d \mathbf{v} : \nabla^d \mathbf{v} d\Omega \quad (24)$$

$$\|q\|_Q^2 := \int_{\Omega} \frac{1}{3\kappa} q^2 d\Omega \quad (25)$$

<sup>197</sup> To establish the relationship between the inf-sup condition and the con-  
<sup>198</sup> straint ratio, the inf-sup condition is firstly transformed by the following Lemma  
<sup>199</sup> 1:

<sup>200</sup> **Lemma 1.** Suppose  $\mathcal{P}_h : V_h \rightarrow Q_h$  is the orthogonal projection operator of the  
<sup>201</sup> divergence operator  $\mathcal{P} := 3\kappa \nabla \cdot$ , i.e.,  $\mathcal{P}_h := 3\kappa \nabla \cdot$  and satisfies Eq. (18). Then,  
<sup>202</sup> the inf-sup value can be estimated by:

$$\beta \leq \inf_{V'_h \subset V_h \setminus \ker \mathcal{P}_h} \sup_{\mathbf{v}_h \in V'_h} \frac{\|\mathcal{P}_h \mathbf{v}_h\|_Q}{\|\mathbf{v}_h\|_V} \quad (26)$$

<sup>203</sup> in which  $\ker \mathcal{P}_h \subset V_h$  is the kernel of  $\mathcal{P}_h$  defined by  $\ker \mathcal{P}_h := \{\mathbf{v}_h \in V_h \mid \mathcal{P}_h \mathbf{v}_h = 0\}$ .

<sup>205</sup> PROOF. First, define the image space of  $\mathcal{P}_h$  as  $\text{Im} \mathcal{P}_h := \{p_h \in Q_h \mid \exists \mathbf{v}_h \in V_h, p_h = \mathcal{P}_h \mathbf{v}_h\}$ . Since  $\mathcal{P}_h \subset Q_h$ , Eq. (23) can be rewritten as:

$$\begin{aligned} \beta &\leq \inf_{q_h \in Q_h} \sup_{\mathbf{v}_h \in V_h} \frac{|b(q_h, \mathbf{v}_h)|}{\|q_h\|_Q \|\mathbf{v}_h\|_V} = \inf_{q_h \in Q_h} \sup_{\mathbf{v}_h \in V_h} \frac{|(q_h, \frac{1}{3\kappa} \mathcal{P} \mathbf{v}_h)|}{\|q_h\|_Q \|\mathbf{v}_h\|_V} \\ &\leq \inf_{q_h \in \text{Im} \mathcal{P}_h} \sup_{\mathbf{v}_h \in V_h} \frac{|\frac{1}{3\kappa} (q_h, \mathcal{P}_h \mathbf{v}_h)|}{\|q_h\|_Q \|\mathbf{v}_h\|_V} \end{aligned} \quad (27)$$

<sup>207</sup> For a given  $q_h \in \text{Im} \mathcal{P}_h$ , since both  $q_h$  and  $\mathcal{P}_h \mathbf{v}_h$  belong to  $\text{Im} \mathcal{P}_h$ ,  $\text{Im} \mathcal{P}_h \subset Q_h$ ,  
<sup>208</sup> according to the Cauchy-Schwarz inequality, we have:

$$\left| \frac{1}{3\kappa} (q_h, \mathcal{P}_h \mathbf{v}_h) \right| \leq \|q_h\|_Q \|\mathcal{P}_h \mathbf{v}_h\|_Q \quad (28)$$

<sup>209</sup> where this equality holds if and only if  $q_h = \mathcal{P}_h \mathbf{v}_h$ , i.e.,

$$\left| \frac{1}{3\kappa} (q_h, \mathcal{P}_h \mathbf{v}_h) \right| = \|q_h\|_Q \|\mathcal{P}_h \mathbf{v}_h\|_Q, \quad \forall \mathbf{v}_h \in V'_h \quad (29)$$

<sup>210</sup> the space  $V'_h \subseteq V_h \setminus \ker \mathcal{P}_h$  defined by:

$$V'_h = \{\mathbf{v}_h \in V_h \mid \mathcal{P}_h \mathbf{v}_h = q_h\} \quad (30)$$

<sup>211</sup> And the following relationship can be evidenced:

$$\sup_{\mathbf{v}_h \in V_h} \frac{|\frac{1}{3\kappa} (q_h, \mathcal{P}_h \mathbf{v}_h)|}{\|q_h\|_Q \|\mathbf{v}_h\|_V} = \sup_{\mathbf{v}_h \in V'_h} \frac{\|\mathcal{P}_h \mathbf{v}_h\|_Q}{\|\mathbf{v}_h\|_V}, \quad \exists q_h \in \text{Im} \mathcal{P}_h \quad (31)$$

<sup>212</sup> Consequently, by combining Eqs. (27) and (31), Eq. (26) can be obtained.

213 **Remark 1.** With Lemma 1 and the norm definitions in Eqs. (24),(25), the  
214 square of the inf-sup value can further be bounded by:

$$\beta^2 \leq \inf_{V'_h \subset V_h \setminus \ker \mathcal{P}_h} \sup_{\mathbf{v}_h \in V'_h} \frac{\|\mathcal{P}_h \mathbf{v}_h\|_Q^2}{\|\mathbf{v}_h\|_V^2} = \inf_{V'_h \subset V_h \setminus \ker \mathcal{P}_h} \sup_{\mathbf{v}_h \in V'_h} \frac{\tilde{a}(\mathbf{v}_h, \mathbf{v}_h)}{a(\mathbf{v}_h, \mathbf{v}_h)} \quad (32)$$

215 The left-hand side of the above equation is consistent with the minimum-maximum  
216 principle [58] and again proves the equivalence with the traditional numerical  
217 inf-sup test [5]. Since that,  $\beta^2$  evaluates the non-zero general eigenvalue of  $\tilde{a}$   
218 and  $a$  in Eq. (22).

### 219 3.2. Inf-sup value estimator

220 Subsequently, the relationship between constraint ratio and the inf-sup con-  
221 dition is established by the following Theorem:

222 **Theorem 1.** Suppose that  $P_{n_u}$  is a complete polynomial space with  $n_u$  dimen-  
223 sions, and  $V_{n_u}$  is the polynomial displacement space,  $V_{n_u} = P_{n_u}^{n_d}$ . The inf-sup  
224 value  $\beta$  can further be bounded by:

$$\beta \leq \beta_s + O(h) \quad (33)$$

225 with

$$\beta_s = \inf_{V' \subset V_{n_u} \setminus \ker \mathcal{P}_h \mathcal{I}_h} \sup_{\mathbf{v} \in V'} \frac{\|\mathcal{P} \mathbf{v}\|_Q}{\|\mathbf{v}\|_V} \quad (34)$$

226 where  $\mathcal{I}_h$  is the interpolation operator of the displacement approximation, and  
227 correspondingly,  $O(h)$  is the remainder related to  $h$ .

228 PROOF. As the dimensions of  $V_h$  and  $V_{n_u}$  are identical,  $\dim V_{n_u} = \dim V_h =$   
229  $n_d \times n_u$ . There exists a unique  $\mathbf{v} \in V_{n_u}$  satisfying  $\mathbf{v}_h = \mathcal{I}_h \mathbf{v}$ . And the right side  
230 of Eq. (26) becomes:

$$\inf_{V'_h \subset V_h \setminus \ker \mathcal{P}_h} \sup_{\mathbf{v}_h \in V'_h} \frac{\|\mathcal{P}_h \mathbf{v}_h\|_Q}{\|\mathbf{v}_h\|_V} = \inf_{V' \subset V_{n_u} \setminus \ker \mathcal{P}_h \mathcal{I}_h} \sup_{\mathbf{v} \in V'} \frac{\|\mathcal{P}_h \mathcal{I}_h \mathbf{v}\|_Q}{\|\mathcal{I}_h \mathbf{v}\|_V} \quad (35)$$

231 According to the triangular inequality, Cauchy-Schwarz inequality, and the  
232 relationship of Eqs. (18), we have:

$$\begin{aligned} \|\mathcal{P}_h \mathcal{I}_h \mathbf{v}\|_Q &= \sup_{q_h \in Q_h} \frac{|\frac{1}{3\kappa}(q_h, \mathcal{P}_h \mathcal{I}_h \mathbf{v})|}{\|q_h\|_Q} = \sup_{q_h \in Q_h} \frac{|\frac{1}{3\kappa}(q_h, \mathcal{P} \mathcal{I}_h \mathbf{v})|}{\|q_h\|_Q} \\ &\leq \sup_{q_h \in Q_h} \frac{|\frac{1}{3\kappa}(q_h, \mathcal{P} \mathbf{v})| + |\frac{1}{3\kappa}(q_h, \mathcal{P} \mathbf{v} - \mathcal{P} \mathcal{I}_h \mathbf{v})|}{\|q_h\|_Q} \\ &\leq \|\mathcal{P} \mathbf{v}\|_Q + \|\mathcal{P}(\mathbf{v} - \mathcal{I}_h \mathbf{v})\|_Q \end{aligned} \quad (36)$$

233 Obviously, the second term on the right side of Eq. (36) is the interpolation  
234 error, and can be evaluated by [59]:

$$\|\mathcal{P}(\mathbf{v} - \mathcal{I}_h \mathbf{v})\|_Q \leq Ch^k |\mathbf{v}|_{H_k} \quad (37)$$

235 where, for a sufficiently smooth  $\mathbf{v} \in V$ ,  $k$  equals to the interpolation order of  
 236  $\mathcal{I}_h$ .

237 Further leading the relation  $\|\mathcal{I}_h \mathbf{v}\|_V \geq C|\mathbf{v}|_{H_k}$  obtained from the closed  
 238 graph theorem [33] and considering Eqs. (36)-(37), the right-hand side of Eq.  
 239 (35) can be represented as:

$$\inf_{V' \subset V_{n_u} \setminus \ker \mathcal{P}_h \mathcal{I}_h} \sup_{\mathbf{v} \in V'} \frac{\|\mathcal{P}_h \mathcal{I}_h \mathbf{v}\|_Q}{\|\mathcal{I}_h \mathbf{v}\|_V} \leq \inf_{V' \subset V_{n_u} \setminus \ker \mathcal{P}_h \mathcal{I}_h} \sup_{\mathbf{v} \in V'} \frac{\|\mathcal{P} \mathbf{v}\|_Q}{\|\mathbf{v}\|_V} + O(h) \quad (38)$$

240 Substituting Eqs. (35),(38) into (26) finally proves Eqs. (33), (34).

241 As we can see in Eqs. (33) and (34),  $\beta_s \geq 0$ , the condition that  $\beta_s$  being  
 242 equal to 0 or not determines whether the formulation can satisfy the inf-sup  
 243 condition. If  $\beta_s > 0$ , as the mesh refines, the second term on the right-hand  
 244 side of Eq. (33) will sharply reduce and can be ignored. In contrast, if  $\beta_s = 0$ ,  
 245 the second term will dominate, and the evaluation of  $\beta$  will be dependent to  $h$ .  
 246 Therefore, the inf-sup condition is violated and numerical instability arises.

### 247 3.3. Polynomial-wise constraint counting

248 From the above subsection, we can know that whether  $\beta_s$  is zero or not  
 249 determines whether the mixed-formulation can fulfill the inf-sup condition. Ac-  
 250 cording to the expression of  $\beta_s$  in Eq. (34), as  $\beta_s = 0$ , the variable  $\mathbf{v}$  should  
 251 belong to  $\ker \mathcal{P}$ , so the dimensions of the subspace in which  $\beta_s \neq 0$ , namely  $n_s$ ,  
 252 can be evaluated by:

$$n_s = \dim(V_{n_u} \setminus \ker \mathcal{P}) \quad (39)$$

253 To further construct the relationship between the inf-sup value estimator in  
 254 Eq. (33) and the constraint ratio  $r = \frac{n_d \times n_u}{n_p}$ , we should find the displacement  
 255 and pressure DOFs in Eq. (33). With the definition of  $V_{n_u}$ , the number of  
 256 displacement DOFs is easy to be evaluated by:

$$n_d \times n_u = \dim V_{n_u} \quad (40)$$

257 With well-posed nodal distributions of displacement and pressure, the number  
 258 of pressure DOFs has the following relationship:

$$n_p = \dim Q_h = \dim(\text{Im} \mathcal{P}_h) = \dim(V_{n_u} \setminus \ker \mathcal{P}_h \mathcal{I}_h) \quad (41)$$

259 Figure 1 illustrates how the relationship between  $n_s$ ,  $n_p$ , and  $n_u$  influences  
 260 the fulfillment of the inf-sup condition:

- 261 • As  $n_p > n_s$ , there must exist a subspace in space  $V_{n_u} \setminus \ker \mathcal{P}_h \mathcal{I}_h$  belonging  
 262 to  $\ker \mathcal{P}$ , resulting in  $\beta_s = 0$ , i.e.,  $V_{n_u} \setminus \ker \mathcal{P}_h \mathcal{I}_h \cap \ker \mathcal{P} \neq \emptyset$ . At this cir-  
 263 cumstance, the inf-sup condition cannot be satisfied, and the formulation  
 264 will suffer from volumetric locking.
- 265 • As  $n_p \leq n_s$ , for well-posed nodal distributions, the space  $V_{n_u} \setminus \ker \mathcal{P}_h \mathcal{I}_h$   
 266 may be a subset of  $V_{n_u} \setminus \ker \mathcal{P}$ . Then,  $\beta_s$  will remain nonzero, and the  
 267 formulation will be locking-free.

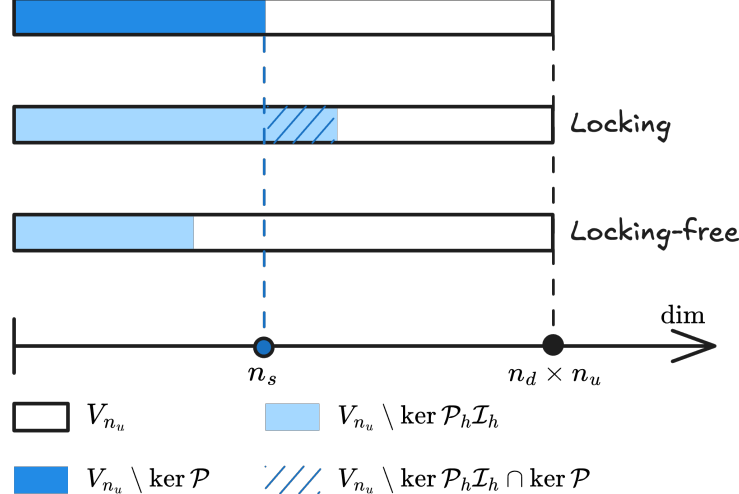


Figure 1: Illustration of estimator

268     Summarily, the formulation can satisfy the inf-sup condition and alleviate  
 269 volumetric locking if at least the number of pressure nodes  $n_p$  is less than  $n_s$ ,  
 270 so we name  $n_s$  as the stabilized number of pressure nodes. At this moment,  
 271 the volumetric constraint ratio should meet the following relation to ensure the  
 272 inf-sup condition:

$$r_{opt} \geq \frac{n_d \times n_u}{n_s} \quad (42)$$

273 **Remark 2.** *Some uniform elements with special arrangements, like the union-*  
 274 *jack element arrangement for 3-node triangular elements, can pass the inf-sup*  
 275 *test [6], but their pressure DOFs number is greater than  $n_s$ . This is because the*  
 276 *union-jack arrangement leads to a lower nonzero eigenvalue number of  $\tilde{a}$  and a*  
 277 *in Eq. (22), and the corresponding nonzero eigenvalue number is less than or*  
 278 *equal to the stabilized number  $n_s$ , satisfying Eq. (42). The similar cases about*  
 279 *this special element arrangement are too few, so it is more straightforward to*  
 280 *use the number of pressure nodes  $n_p$  to measure  $\dim(V_{n_u} \setminus \ker \mathcal{P}_h \mathcal{I}_h)$ .*

281 **Remark 3.** *It is obvious that the traditional optimal constraint ratio cannot*  
 282 *fulfill this condition. However, not all formulations satisfying this condition can*  
 283 *totally avoid volumetric locking. This is because  $n_p \leq n_s$  is not equivalent to*  
 284  *$V_{n_u} \setminus \ker \mathcal{P}_h \mathcal{I}_h \subset V_{n_u} \setminus \ker \mathcal{P}$ . Fortunately, well-posed nodal distributions of*  
 285 *displacement and pressure can ensure this, which will be evidenced by numerical*  
 286 *examples in the subsequent sections.*

### 287 3.4. Optimal volumetric constraint ratio

288     The fulfillment of the inf-sup condition should require the number of pres-  
 289 sure nodes  $n_p$  to be lower than the stabilized number  $n_s$ , and now, we will  
 290 demonstrate how to determine  $n_s$  for a specific number of displacement DOFs.

<sup>291</sup> In the 2D case, for instance, we first consider the linear polynomial displace-  
<sup>292</sup> ment space  $V_3$  that is given by:

$$V_3 = \text{span} \left\{ \begin{pmatrix} 1 \\ 0 \end{pmatrix}, \begin{pmatrix} 0 \\ 1 \end{pmatrix}, \begin{pmatrix} x \\ 0 \end{pmatrix}, \begin{pmatrix} 0 \\ x \end{pmatrix}, \begin{pmatrix} y \\ 0 \end{pmatrix}, \begin{pmatrix} 0 \\ y \end{pmatrix} \right\} \quad (43)$$

<sup>293</sup> or rearranged as follows,

$$V_3 = \text{span} \left\{ \underbrace{\begin{pmatrix} 1 \\ 0 \end{pmatrix}, \begin{pmatrix} 0 \\ 1 \end{pmatrix}, \begin{pmatrix} y \\ 0 \end{pmatrix}, \begin{pmatrix} 0 \\ x \end{pmatrix}, \begin{pmatrix} x \\ -y \end{pmatrix}}_{\ker \mathcal{P}}, \underbrace{\begin{pmatrix} x \\ y \end{pmatrix}}_{V_3 \setminus \ker \mathcal{P}} \right\} \quad (44)$$

<sup>294</sup> It can be counted that, for  $n_u = 3$ ,  $n_s = 1$ . Following the path, the displacement  
<sup>295</sup> space with a quadratic polynomial base, namely  $V_6$ , can be stated as:

$$V_6 = \text{span} \left\{ \underbrace{\begin{pmatrix} 1 \\ 0 \end{pmatrix}, \begin{pmatrix} 0 \\ 1 \end{pmatrix}, \begin{pmatrix} y \\ 0 \end{pmatrix}, \begin{pmatrix} 0 \\ x \end{pmatrix}, \begin{pmatrix} x \\ -y \end{pmatrix}, \begin{pmatrix} x^2 \\ -2xy \end{pmatrix}, \begin{pmatrix} y^2 \\ 0 \end{pmatrix}, \begin{pmatrix} 0 \\ x^2 \end{pmatrix}, \begin{pmatrix} -2xy \\ y^2 \end{pmatrix}}_{\ker \mathcal{P}}, \underbrace{\begin{pmatrix} x \\ y \end{pmatrix}, \begin{pmatrix} x^2 \\ 2xy \end{pmatrix}, \begin{pmatrix} 2xy \\ y^2 \end{pmatrix}}_{V_6 \setminus \ker \mathcal{P}} \right\} \quad (45)$$

<sup>296</sup> In this circumstance,  $n_s = 3$ . As the order of the polynomial space increases,  
<sup>297</sup> the optimal numbers of constraint DOFs for each order of the polynomial space  
<sup>298</sup> are listed in Table. 1, in which  $n$  denotes the order of space  $P_{n_u}$ . For the  
<sup>299</sup> flexibility of usage, the relation between  $n_u$  and  $n_s$  is summarized as follows:

$$n_s = \frac{n(n+1)}{2}, \quad n = \left\lfloor \frac{\sqrt{1+8n_u}-3}{2} \right\rfloor \quad (46)$$

<sup>300</sup> where  $\lfloor \bullet \rfloor$  denotes the floor function.

Table 1: Relationship between the number of displacement nodes  $n_u$  and stabilized number of pressure nodes  $n_s$

$n$	2D		3D	
	$n_u$	$n_s$	$n_u$	$n_s$
1	3	1	4	1
2	6	3	10	4
3	10	6	20	10
4	15	10	35	20
$\vdots$	$\vdots$	$\vdots$	$\vdots$	$\vdots$

<sup>301</sup> For the 3D case, following the path in 2D, the linear polynomial space  $V_4$  is

302 considered herein, and the arranged space of  $V_4$  is listed as follows:

$$V_4 = \text{span} \left\{ \underbrace{\begin{pmatrix} 1 \\ 0 \\ 0 \\ 0 \end{pmatrix}, \begin{pmatrix} 0 \\ 1 \\ 0 \\ 0 \end{pmatrix}, \begin{pmatrix} 0 \\ 0 \\ 1 \\ 0 \end{pmatrix}}_{\ker \mathcal{P}}, \underbrace{\begin{pmatrix} 0 \\ x \\ 0 \\ 0 \end{pmatrix}, \begin{pmatrix} 0 \\ 0 \\ x \\ 0 \end{pmatrix}, \begin{pmatrix} 0 \\ 0 \\ 0 \\ y \end{pmatrix}}_{\ker \mathcal{P}}, \underbrace{\begin{pmatrix} 0 \\ 0 \\ z \\ 0 \end{pmatrix}, \begin{pmatrix} 0 \\ 0 \\ 0 \\ z \end{pmatrix}, \begin{pmatrix} x \\ -y \\ 0 \\ 0 \end{pmatrix}, \begin{pmatrix} x \\ 0 \\ -z \\ z \end{pmatrix}}_{V_{n_u} \setminus \ker \mathcal{P}} \right\} \quad (47)$$

303 For brevity, the stabilized numbers for higher-order polynomial displacement  
 304 spaces are directly listed in Table. 1, and it can be summarized that, for a given  
 305 number of displacement DOFs, the stabilized number for pressure DOFs can be  
 306 calculated as follows:

$$n_s = \frac{n(n+1)(n+2)}{6} \quad (48)$$

$$n = \left[ \left( 3n_u + \frac{1}{3} \sqrt{81n_u^2 - \frac{1}{3}} \right)^{\frac{1}{3}} + \frac{1}{3 \left( 3n_u + \frac{1}{3} \sqrt{81n_u^2 - \frac{1}{3}} \right)^{\frac{1}{3}}} - 2 \right] \quad (49)$$

307 Table 2 lists the effectiveness of the traditional constraint ratio and the  
 308 proposed optimal constraint ratio for traditional mixed formulation schemes,  
 309 comparing the constraint ratios with the fulfillment of the inf-sup condition  
 310 using analytical proof and numerical prediction. The table reveals that the  
 311 traditional constraint ratio  $r \geq n_d$  is not sufficient to guarantee the inf-sup  
 312 condition, especially for Q4P1 and Q8P3. The proposed optimal constraint  
 313 ratio  $r_{opt} \geq \frac{n_d \times n_u}{n_s}$  is more effective in ensuring the inf-sup condition, since the  
 314 corresponding results is consistent with numerical prediction or analytical proof  
 315 of inf-sup condition.

#### 316 4. Mixed FE–meshfree formulation with optimal constraint ratio

317 In the proposed mixed–formulation, the displacement is approximated using  
 318 3-node (Tri3), 6-node (Tri6) triangular elements and 4-node (Quad4), 8-node  
 319 (Quad8) quadrilateral elements in 2D, 4-node (Tet4) tetrahedral element and  
 320 8-node (Hex8) hexahedral element in 3D [2]. In order to flexibly adjust to let  
 321 the DOFs of pressure meet the optimal constraint, the reproducing kernel (RK)  
 322 meshfree approximation is involved to approximate pressure, namely FE–RK  
 323 formulation.

##### 324 4.1. Reproducing kernel meshfree approximation

325 In accordance with the reproducing kernel approximation, the entire domain  
 326  $\Omega$ , as shown in Figure 2, is discretized by  $n_p$  meshfree nodes,  $\{\mathbf{x}_I\}_{I=1}^{n_p}$ . The

Table 2: Inf-sup condition and constraint ratio for various mixed formulations

Formulation	Inf-sup condition		$r \geq n_d$	$r = r_{opt}$
	Numerical prediction	Analytical proof		
T3P1( $r = 1$ )	✗	✗	✗	✗
Q4P1( $r = 2$ )	✗	✗	✓	✗
Q8P3( $r = 2$ )	✗	✗	✓	✗
Q8P1( $r = 6$ )	✓	✓	✓	✓
Q9P3( $r = \frac{8}{3}$ )	✓	✓	✓	✓
MINI( $r = 6$ )	✓	✓	✓	✓
Taylor-Hood( $r = 8$ )	✓	✓	✓	✓
T6C3( $r = 8$ )	✓	✓		✓

● :Displacement node    ● :Pressure node

<sup>327</sup> approximated pressure, namely  $p_h$ , can be expressed by the shape function  $\Psi_I$   
<sup>328</sup> and nodal coefficient  $p_I$ , yields:

$$p_h(\mathbf{x}) = \sum_{I=1}^{n_p} \Psi_I(\mathbf{x}) p_I \quad (50)$$

<sup>329</sup> where, in the reproducing kernel approximation framework, the shape function  
<sup>330</sup>  $\Psi_I$  is given by:

$$\Psi_I(\mathbf{x}) = \mathbf{c}(\mathbf{x}_I - \mathbf{x}) \mathbf{p}(\mathbf{x}_I - \mathbf{x}) \phi(\mathbf{x}_I - \mathbf{x}) \quad (51)$$

<sup>331</sup> in which  $\mathbf{p}$  is the basis vector, for instance in the context of the 3D quadratic  
<sup>332</sup> case, the basis vector takes the following form:

$$\mathbf{p}(\mathbf{x}) = \{1, x, y, z, x^2, y^2, z^2, xy, xz, yz\}^T \quad (52)$$

<sup>333</sup> and  $\phi$  stands for the kernel function. In this work, the traditional Cubic B-spline  
<sup>334</sup> function with square or cube support is used as the kernel function:

$$\phi(\mathbf{x}_I - \mathbf{x}) = \phi(s_x) \phi(s_y) \phi(s_z), \quad s_i = \frac{\|\mathbf{x}_I - \mathbf{x}\|}{\bar{s}_{iI}} \quad (53)$$

<sup>335</sup> with

$$\phi(s) = \frac{1}{3!} \begin{cases} (2-2s)^3 - 4(1-2s)^3 & s \leq \frac{1}{2} \\ (2-2s)^3 & \frac{1}{2} < s < 1 \\ 0 & s > 1 \end{cases} \quad (54)$$

<sup>336</sup> where  $\bar{s}_{iI}$ 's are the support size towards the  $i$ -direction for the shape function  
<sup>337</sup>  $\Psi_I$ . The correction function  $\mathbf{c}$  can be determined by the following so-called  
<sup>338</sup> consistency condition:

$$\sum_{I=1}^{n_p} \Psi_I(\mathbf{x}) \mathbf{p}(\mathbf{x}_I) = \mathbf{p}(\mathbf{x}) \quad (55)$$

<sup>339</sup> or equivalent shifted form:

$$\sum_{I=1}^{n_p} \Psi_I(\mathbf{x}) \mathbf{p}(\mathbf{x}_I - \mathbf{x}) = \mathbf{p}(\mathbf{0}) \quad (56)$$

<sup>340</sup> The consistency condition ensures that the reproducing kernel shape functions  
<sup>341</sup> are able to reproduce the polynomial space spanned by the basis function  $\mathbf{p}$ ,  
<sup>342</sup> which is a fundamental requirement for the accuracy of the Galerkin method.  
<sup>343</sup> Herein, the order of the basis function  $\mathbf{p}$  is chosen to be the same as the order  
<sup>344</sup> of the displacement approximation.

<sup>345</sup> Further, substituting Eq. 51 into Eq. (56) leads to:

$$\mathbf{c}(\mathbf{x}_I - \mathbf{x}) = \mathbf{A}^{-1}(\mathbf{x}_I - \mathbf{x}) \mathbf{p}(\mathbf{0}) \quad (57)$$

<sup>346</sup> in which  $\mathbf{A}$  is namely the moment matrix evaluated by:

$$\mathbf{A}(\mathbf{x}_I - \mathbf{x}) = \sum_{I=1}^{n_p} \mathbf{p}(\mathbf{x}_I - \mathbf{x}) \mathbf{p}^T(\mathbf{x}_I - \mathbf{x}) \phi(\mathbf{x}_I - \mathbf{x}) \quad (58)$$

<sup>347</sup> Taking Eq. (57) back to Eq. (51), the final form of the reproducing kernel shape  
<sup>348</sup> function can be obtained as:

$$\Psi_I(\mathbf{x}) = \mathbf{p}^T(\mathbf{0})\mathbf{A}^{-1}(\mathbf{x}_I - \mathbf{x})\phi(\mathbf{x}_I - \mathbf{x}) \quad (59)$$

<sup>349</sup> As shown in Figure 2, reproducing kernel meshfree shape functions are glob-  
<sup>350</sup> ally smooth across the entire domain, using them to discretize the pressure field  
<sup>351</sup> allows the constraint ratio to be adjusted arbitrarily, without being limited by  
<sup>352</sup> element topology. Meshfree shape functions generally lack the Kronecker delta  
<sup>353</sup> property, which prevents the direct imposition of essential boundary conditions.  
<sup>354</sup> Fortunately, the mixed formulation shown in Eq. 14 only concerns the displace-  
<sup>355</sup> ment essential boundary condition, and this condition can be easily imposed by  
<sup>356</sup> the standard methods, such as the penalty method that used in this work.

<sup>357</sup> Moreover, when combined with finite element approximations in Eq. 14,  
<sup>358</sup> numerical integration can be conveniently performed within each finite element  
<sup>359</sup> ( $\Omega_C$ 's). The numerical integration issue caused by the loss of variational con-  
<sup>360</sup> sistency between meshfree shape functions and their derivatives [60] would not  
<sup>361</sup> appear in the mixed formulation of Eq. 14, this is due to the fact that Eq.  
<sup>362</sup> 14 solely depends on the meshfree shape functions themselves. Therefore, the  
<sup>363</sup> proposed method employs standard lower-order Gaussian quadrature rules, as  
<sup>364</sup> commonly used in traditional finite element methods, while still maintaining its  
<sup>365</sup> accuracy. Table 3 lists the integration schemes used in this work for mixed-  
<sup>366</sup> formulations. Methods with linear basis functions use an integration scheme of  
<sup>367</sup> order 2. Those with quadratic basis functions use a scheme of order 4. The  
<sup>368</sup> detailed locations and weights of the Gauss points can be found in Ref. [4]. A  
<sup>369</sup> sensitivity study on the integration order is carried out in a further numerical  
<sup>370</sup> example in Section 5.2. The results from this study demonstrate the efficacy of  
<sup>371</sup> these integration schemes.

Table 3: Integration schemes for the mixed FE–meshfree formulation

Methods	$n_o$	$n_g$ for $\Omega$	$n_g$ for $\Gamma$
Tri3-RK	2	3	2
Tri6-RK	4	6	3
Quad4-RK	2	$2 \times 2$	2
Quad8-RK	4	$3 \times 3$	3
Tet4-RK	2	4	3
Hex8-RK	2	$2 \times 2 \times 2$	4

$n_o$ : Integration Order     $n_g$ : Number of integration points

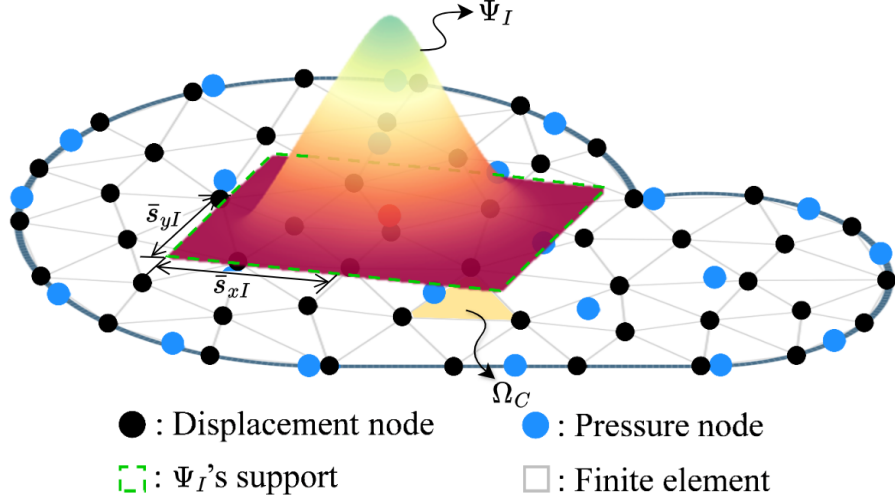


Figure 2: Illustration for reproducing kernel meshfree approximation

<sup>372</sup> *4.2. Pressure node distributions with optimal constraint ratio*

<sup>373</sup> In this subsection, 2D and 3D inf-sup tests [6], as defined in Eq. 32, are  
<sup>374</sup> conducted using the mixed FE-meshfree formulations to validate the proposed  
<sup>375</sup> inf-sup value estimator. The 2D test considers the square domain  $\Omega = (0, 1) \times$   
<sup>376</sup>  $(0, 1)$ , where the displacement is discretized by Tri3 and Quad4 with  $4 \times 4$ ,  
<sup>377</sup>  $8 \times 8$ ,  $16 \times 16$  and  $32 \times 32$  elements, Tri6 and Quad8 with  $2 \times 2$ ,  $4 \times 4$ ,  $8 \times 8$   
<sup>378</sup> and  $16 \times 16$  elements, respectively. The 3D test employs a cube domain  $\Omega =$   
<sup>379</sup>  $(0, 1) \times (0, 1) \times (0, 1)$  with  $4 \times 4$ ,  $8 \times 8$  and  $16 \times 16$  elements for the Tet4 and Hex8.  
<sup>380</sup> For pressure discretization, linear meshfree approximation with a normalized  
<sup>381</sup> support size of 1.5 is employed for Tri3, Quad4, Tet4 and Hex8. For Tri6 and  
<sup>382</sup> Quad8, a quadratic meshfree approximation with a normalized support size of  
<sup>383</sup> 2.5 is utilized. In order to avoid the influence of interpolation error, uniform  
<sup>384</sup> nodal distributions are used for pressure discretizations, for example in Figure  
<sup>385</sup> 3, which displays  $4 \times 4$  Quad4 elements with  $4 \times 3$  uniformly distributed pressure  
<sup>386</sup> nodes.

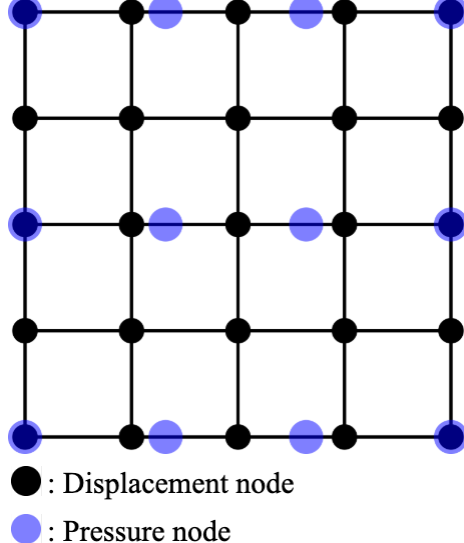


Figure 3: Illustration of uniform nodal distribution for inf-sup test with  $n_u = 5 \times 5$ ,  $n_p = 4 \times 3$

Figures 4–9 show the corresponding results, in which the red line stands for the value of  $\beta$  with respect to the number of pressure nodes  $n_p$ , and the vertical dashed line denotes the stabilized number  $n_s$ . The deeper color of the lines means mesh refinement. The results show that, no matter linear or quadratic elements, as  $n_p$  increases over  $n_s$ , the value of  $\beta$  sharply decreases, and then the inf-sup condition cannot be maintained. This result is consistent with the discussion in Section 3, and again verifies the effect of the proposed estimator.

Moreover, the mixed formulation's results with the traditional optimal constraint ratio  $r = n_d$  are listed in these figures as well, and  $\beta$  in this circumstance is already much smaller than those in the optimal range. Considering the results shown above, the easy programming and efficiency, the pressure nodes are chosen among the displacement nodes. The optimal schemes for linear and quadratic, 2D and 3D element discretizations, namely with  $r = r_{opt}$ , are shown in Figure 10, where every other displacement node is selected as the pressure node. For practical implementations of linear cases, the pressure nodes are initially generated using traditional approaches, such as Delaunay triangulation. Subsequently, the displacement nodes are then obtained through a standard mesh refinement process to the pressure nodes. For quadratic approximations in Tri6 and Quad8 elements, the element vertices are chosen as pressure nodes after displacement element generation. Consequently, all constraint ratios evaluated using the discretizations in Figure 10 fall within the optimal range. The corresponding inf-sup test results for these schemes are also marked in inf-sup test figure and show that, with mesh refinement, their  $\beta$ 's are always maintained at a non-negligible level.

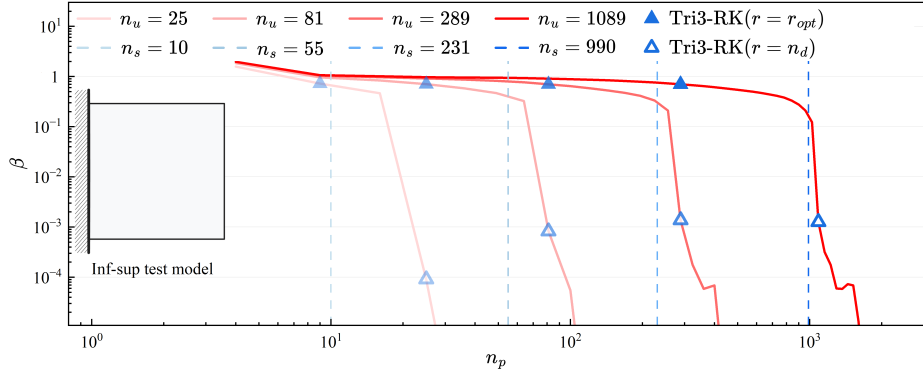


Figure 4: Inf-sup test for Tri3-RK

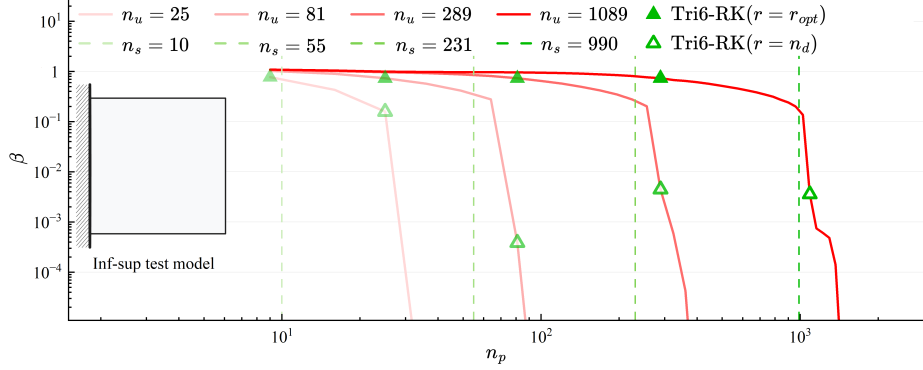


Figure 5: Inf-sup test for Tri6-RK

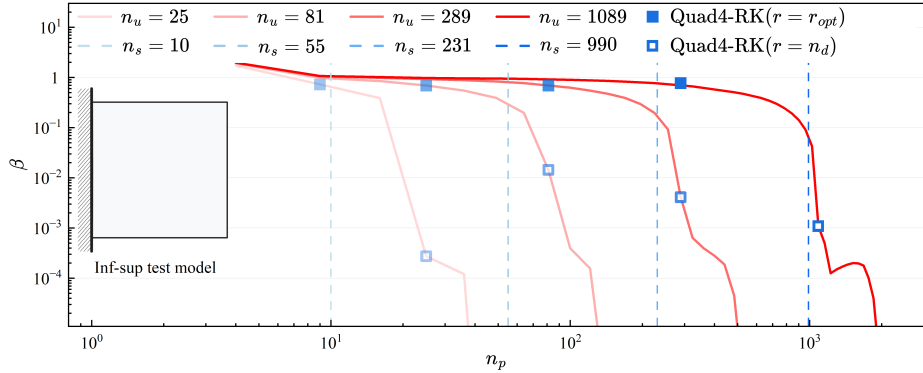


Figure 6: Inf-sup test for Quad4-RK

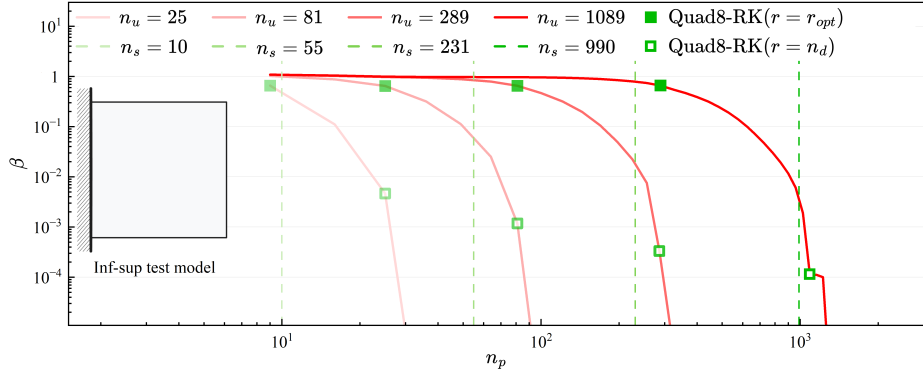


Figure 7: Inf-sup test for Quad8-RK

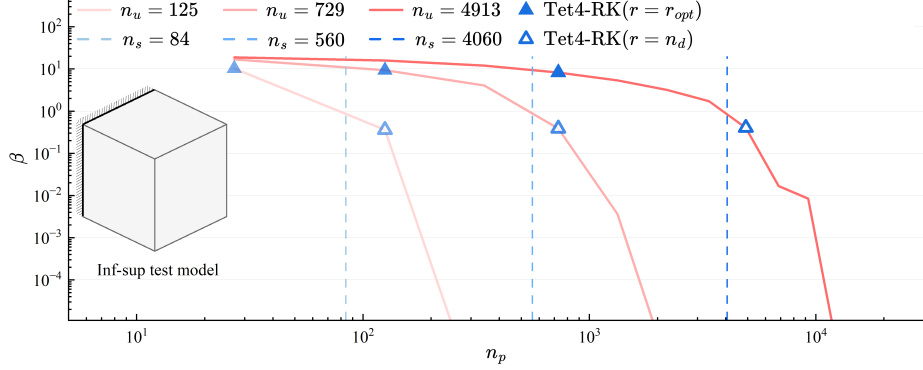


Figure 8: Inf-sup test for Tet4-RK

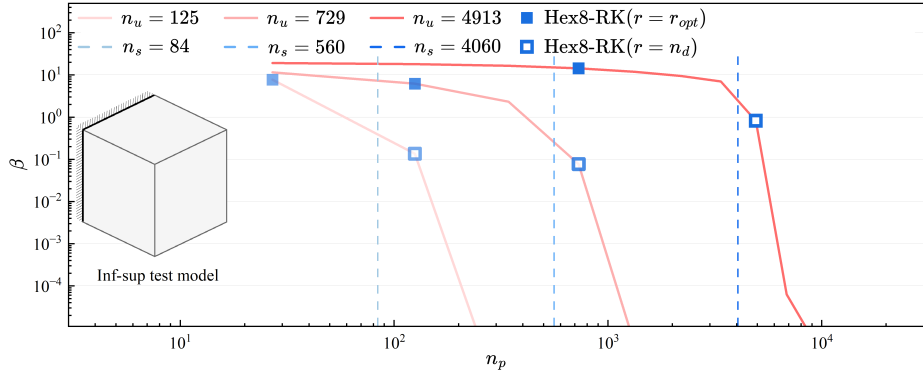


Figure 9: Inf-sup test for Hex8-RK

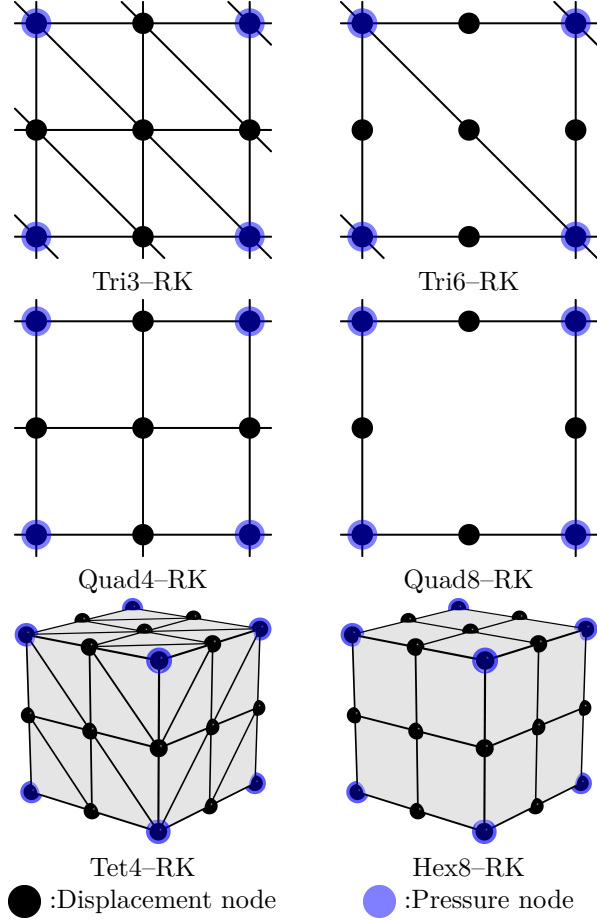


Figure 10: Nodal distribution schemes for mixed FE-meshfree formulations with  $r = r_{opt}$

## 411 5. Numerical examples

### 412 5.1. Cantilever beam problem

413 Consider the cantilever beam problem shown in Figure 11 with length  $L =$   
 414  $D = 12$ , and the incompressible material parameters are employed  
 415 with Young's modulus  $E = 3 \times 10^6$ , Poisson's ratio  $\nu = 0.5 - 10^{-8}$ . The left hand  
 416 side is fixed and the right side subject to a concentrated force  $P = 1000$ . All  
 417 the prescribed values in the boundary conditions are evaluated by the analytical  
 418 solution that is given as follows [61]:

$$\begin{cases} u_x(\mathbf{x}) = -\frac{Py}{6EI} \left( (6L - 3x)x + (2 + \bar{\nu})(y^2 - \frac{D^2}{4}) \right) \\ u_y(\mathbf{x}) = \frac{P}{6EI} \left( 3\bar{\nu}y^2(L - x) + (4 + 5\bar{\nu})\frac{D^2x}{4} + (3L - x)x^2 \right) \end{cases} \quad (60)$$

<sup>419</sup> where  $I$  is the beam's moment of inertia,  $\bar{E}$  and  $\bar{\nu}$  are the material parameters  
<sup>420</sup> for plane strain hypothesis, they can be expressed by:

$$I = \frac{D^3}{12}, \quad \bar{E} = \frac{E}{1 - \nu^2}, \quad \bar{\nu} = \frac{\nu}{1 - \nu} \quad (61)$$

<sup>421</sup> And correspondingly, the stress components and the pressure are evaluated by

$$\begin{cases} \sigma_{xx} = -\frac{P(L-x)y}{I} \\ \sigma_{yy} = 0 \\ \sigma_{xy} = \frac{P}{2I}\left(\frac{D^2}{4} - y^2\right) \\ p = -\frac{P(1+\nu)(L-x)y}{3I} \end{cases} \quad (62)$$

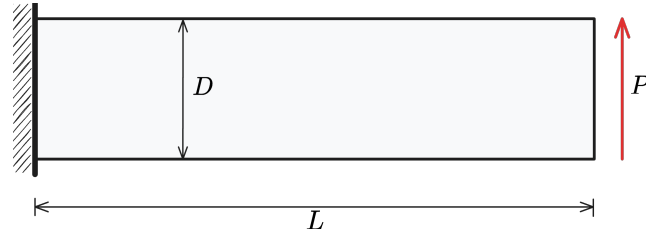


Figure 11: Illustration of cantilever beam problem

<sup>422</sup> In this problem, the Tri3, Quad4 elements with  $16 \times 4$ ,  $32 \times 8$ ,  $64 \times 16$ ,  $128 \times 32$   
<sup>423</sup> grids, and Tri6, Quad8 elements with  $8 \times 2$ ,  $16 \times 4$ ,  $32 \times 8$ ,  $64 \times 16$  grids are  
<sup>424</sup> employed for displacement discretization. The pressure is discretized by linear  
<sup>425</sup> and quadratic meshfree approximations with 1.5 and 2.5 characterized support  
<sup>426</sup> sizes respectively. The strain and pressure errors with respect to pressure nodes  
<sup>427</sup>  $n_p$  are displayed in Figures 12, 13, where, to avoid the interpolation error, the  
<sup>428</sup> pressure nodes are uniformly distributed independent with displacement nodes  
<sup>429</sup> by the same way in Section 4.2. The vertical dashed lines stand for the stabilized  
<sup>430</sup> number  $n_s$ . The figures imply that all pressure errors immediately increase when  
<sup>431</sup> their constraint ratios are out of the optimal range, and quadratic elements still  
<sup>432</sup> have better results than linear elements. It is interesting that the pressure errors  
<sup>433</sup> do not increase as  $n_p$  becomes very small. This is because the exact pressure  
<sup>434</sup> solution for this problem, given in Eq. (62), is only a second-order polynomial.  
<sup>435</sup> Consequently, the pressure interpolation error in Eq. (A.14) is either very small  
<sup>436</sup> or nonexistent. In this circumstance, the pressure interpolation error is primarily  
<sup>437</sup> controlled by strain error and inf-sup value  $\beta$ . For the strain error, the Quad8-  
<sup>438</sup> RK method shows stable results regardless of whether the constraint ratio is in  
<sup>439</sup> the optimal range. This may be due to the fact that the Quad8 element with a  
<sup>440</sup> regular mesh satisfies the relationship of Eq. (A.16). In this context, the strain

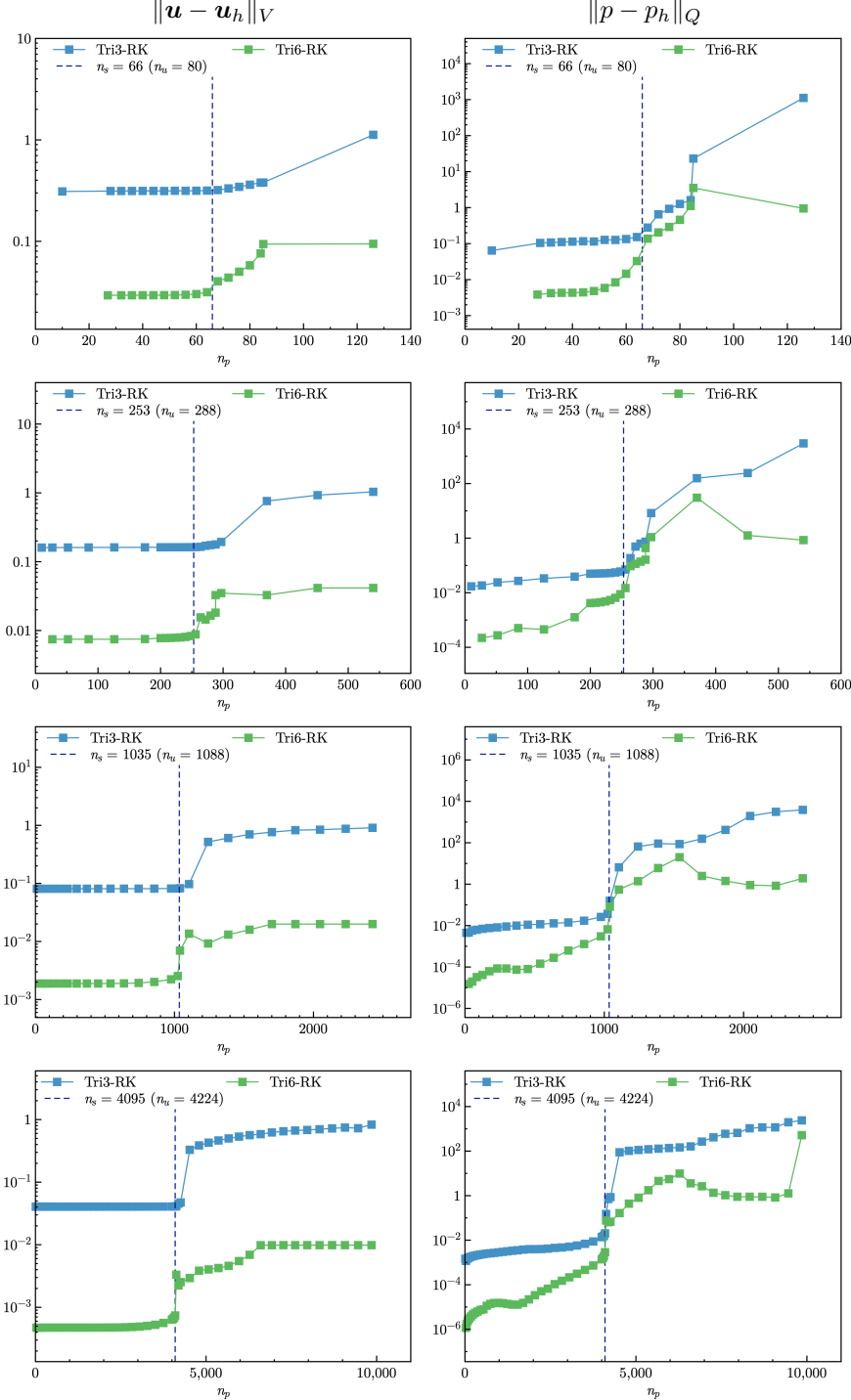


Figure 12: Strain and pressure errors vs.  $n_p$  for cantilever beam problem with triangular elements

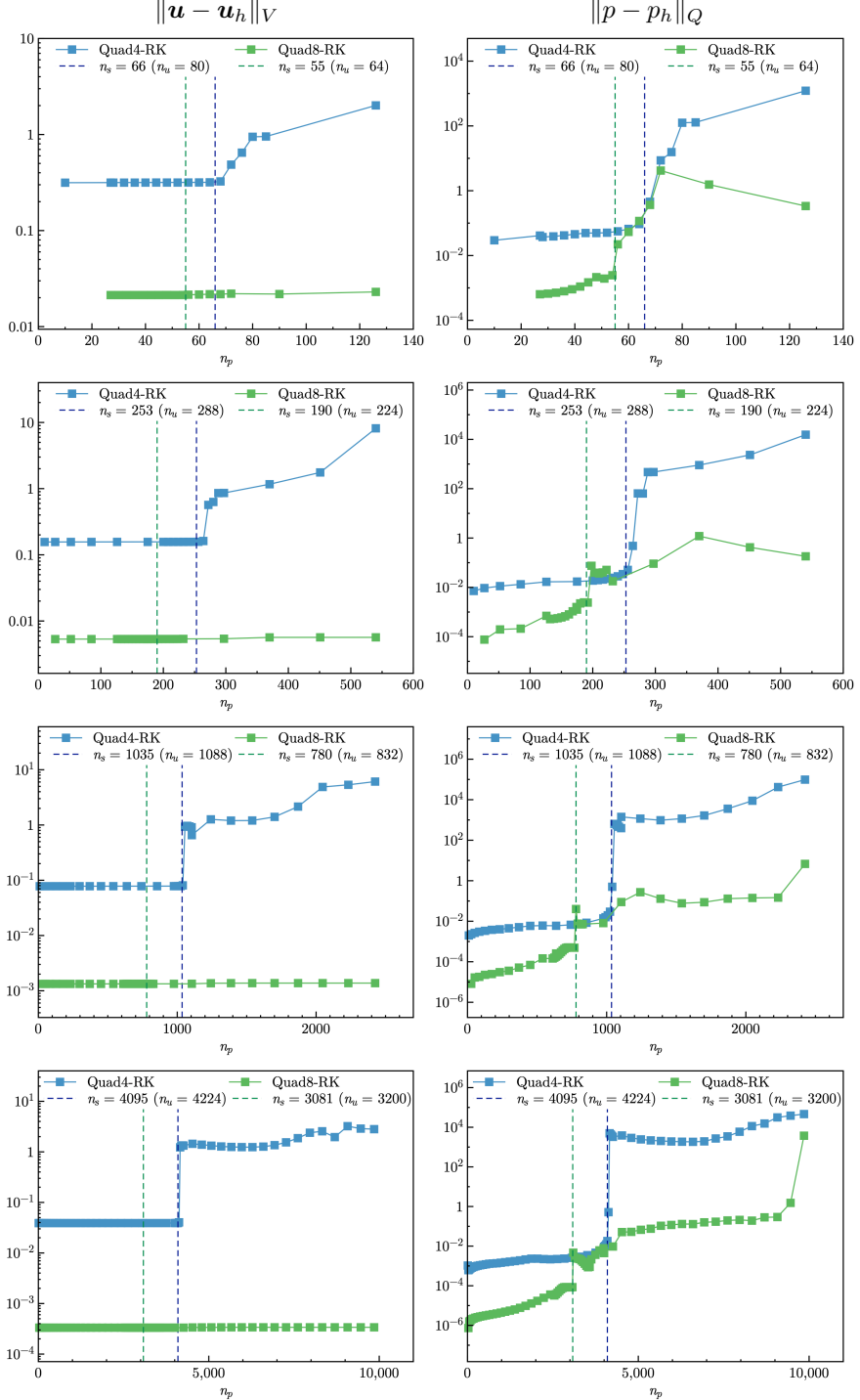


Figure 13: Strain and pressure errors vs.  $n_p$  for cantilever beam problem with quadrilateral elements

441 error of Eq. (A.10) is independent of the inf-sup value  $\beta$  and remains at a low  
 442 level.

443 To further investigate the performance of proposed methods in unstructured  
 444 mesh, a non-uniform discretization version of the study on strain and pressure  
 445 errors with respect to  $n_p$  is conducted shown in Figure 14. Accordingly, the  
 446 pressure nodes are also non-uniformly distributed and independent of the dis-  
 447 placement nodes. The related results, shown in Figure 15, imply that all errors  
 448 increase more rapidly as the constraint ratio falls outside the optimal range.  
 449 The quadratic approximations, Tri6-RK and Quad8-RK, demonstrate better  
 450 performance in resisting volumetric locking. In this case, the increase in Tri6-  
 451 RK's strain and pressure errors has a gentler slope when the number of pressure  
 452 nodes exceeds  $n_s$ .

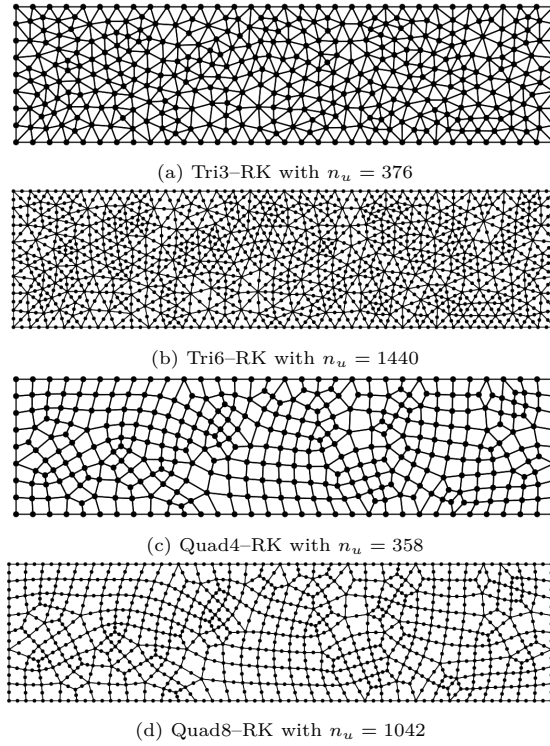


Figure 14: Non-uniform discretizations for cantilever beam problem

453 Figures 16, 17 are the strain and pressure error convergence studies for tri-  
 454 angular and quadrilateral elements, respectively, in which Tri3-RK, Tri6-RK  
 455 with  $r = n_d$ , the MINI element [32], 6-node triangular displacement element  
 456 with 3-node continuous triangular pressure element (T6C3) are the comparative  
 457 methods for Tri3-RK and Tri6-RK with  $r = r_{opt}$ , and Quad4-RK, Quad8-RK  
 458 with  $r = n_d$ , 4-node quadrilateral displacement element with 1-node piecewise  
 459 constant pressure (Q4P1), 8-node quadrilateral displacement element with 3-

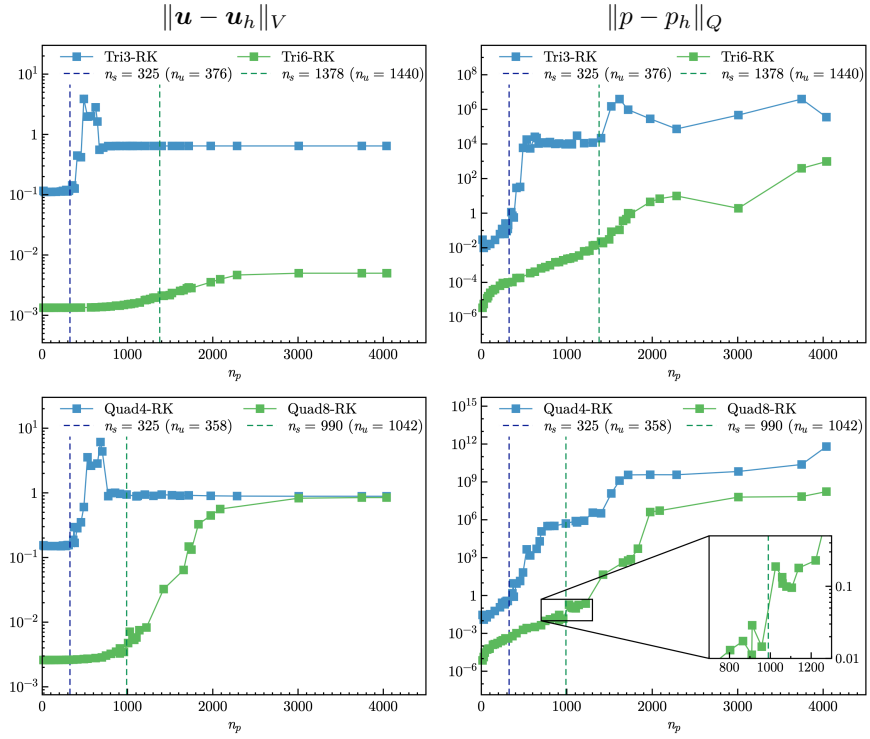


Figure 15: Strain and pressure errors vs.  $n_p$  for cantilever beam problem with non-uniform discretizations

node piecewise linear pressure (Q8P3) are employed for comparison with Quad4–RK and Quad8–RK with  $r = r_{opt}$ . Except Tri3–RK, Quad8–RK with  $r = n_d$  for strain error, all formulations with the traditional constraint ratio of  $r = n_d$  cannot ensure the optimal error convergence rates. The proposed mixed formulations with  $r = r_{opt}$  can maintain the optimal error convergence ratio, except the strain error of Quad8–RK is a little larger than that of Q8P3, the proposed approaches show the best performance in accuracy.

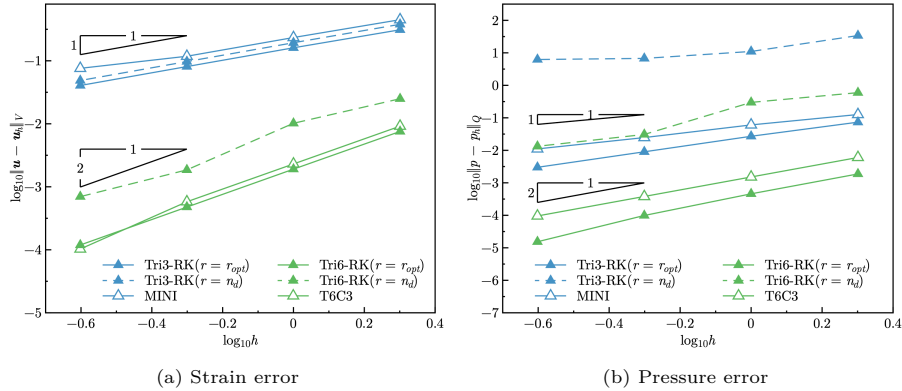


Figure 16: Error convergence study for cantilever beam problem with triangular elements

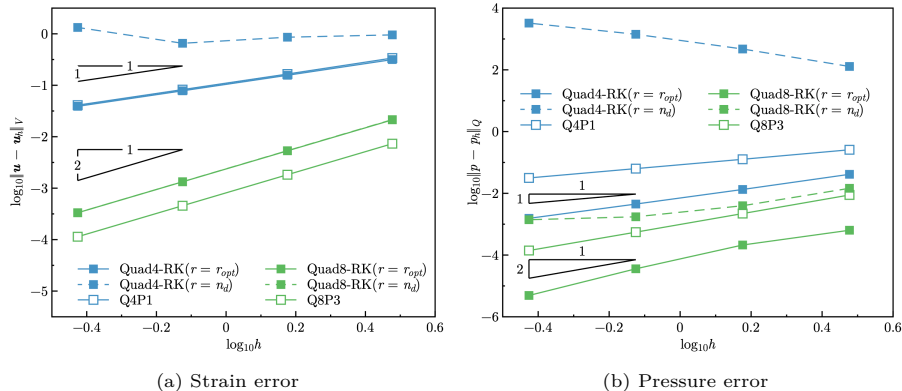


Figure 17: Error convergence study for cantilever beam problem with quadrilateral elements

### 5.2. Plate with hole problem

Consider an infinite plate with a hole centered at the origin, as shown in Figure 18, and at the infinity towards the  $x$ -direction subjected to a uniform traction  $T = 1000$ . The geometric and material parameters for this problem are that the ratio of the hole  $a = 1$ , Young's modulus  $E = 3 \times 10^6$ , and Poisson's ratio  $\nu = 0.5 - 10^{-8}$ . The analytical solution of this problem refers to the

<sup>473</sup> Michell solution [61] as:

$$\begin{cases} u_x(\rho, \theta) = \frac{Ta}{8\mu} \left( \frac{\rho}{a}(k+1) \cos \theta - \frac{2a^3}{\rho^3} \cos 3\theta + \frac{2a}{\rho} ((1+k) \cos \theta + \cos 3\theta) \right) \\ u_y(\rho, \theta) = \frac{Ta}{8\mu} \left( \frac{\rho}{a}(k-3) \sin \theta - \frac{2a^3}{\rho^3} \sin 3\theta + \frac{2a}{\rho} ((1-k) \sin \theta + \sin 3\theta) \right) \end{cases} \quad (63)$$

<sup>474</sup> in which  $k = \frac{3-\nu}{1+\nu}$ ,  $\mu = \frac{E}{2(1+\nu)}$ . And the stress components are given by:

$$\begin{cases} \sigma_{xx} = T \left( 1 - \frac{a^2}{\rho^2} \left( \frac{3}{2} \cos 2\theta + \cos 4\theta \right) + \frac{3a^4}{2\rho^4} \cos 4\theta \right) \\ \sigma_{yy} = -T \left( \frac{a^2}{\rho^2} \left( \frac{1}{2} \cos 2\theta - \cos 4\theta \right) + \frac{3a^4}{2\rho^4} \cos 4\theta \right) \\ \sigma_{xy} = -T \left( \frac{a^2}{\rho^2} \left( \frac{1}{2} \sin 2\theta + \sin 4\theta \right) - \frac{3a^4}{2\rho^4} \sin 4\theta \right) \end{cases} \quad (64)$$

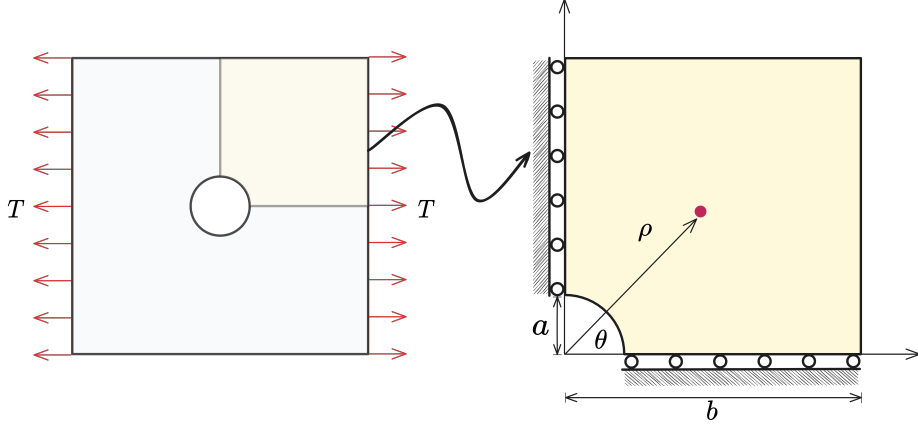


Figure 18: Illustration of plate with hole problem

<sup>475</sup> According to the symmetry property of this problem, only a quarter model  
<sup>476</sup> with length  $b = 5$  is considered as shown in Figure 18. The displacement is  
<sup>477</sup> discretized by 3-node, 6-node triangular elements, 4-node and 8-node quadrilateral elements.  
<sup>478</sup> The corresponding linear and quadratic meshfree formulations are employed for pressure discretization, and the characterized support sizes  
<sup>479</sup> are chosen as 1.5 and 2.5, respectively. Figures 19, 20 study the relationship  
<sup>480</sup> between strain, pressure errors, and  $n_p$  using the nodal distributions uniformly  
<sup>481</sup> related to displacement nodes. Unlike the quadrilateral element case in Section  
<sup>482</sup> 5.1, both displacement and pressure errors in this problem increase as  $n_p$  reduces  
<sup>483</sup> to a small value. Tri3-RK exhibits less sensitivity in strain error than Tri6-RK.  
<sup>484</sup> This is because, as shown in Eqs. (A.10) and (A.20), the displacement approx-  
<sup>485</sup> imation error for the space of  $\ker \mathcal{P}_h$  does not increase as immediately when  $\frac{C_b}{\beta}$

487 in Eq. (A.20) is not too much larger than 1. However, its error increases as  $n_p$   
488 goes up. Both FE-RK with constraint ratios under the optimal range perform  
489 acceptably.

490 The corresponding error convergence studies are presented in Figures 21,  
491 22, the results show that only Tri3-RK with  $r = 2$  shows a comparable strain  
492 error with the optimal one with  $r = r_{opt}$  in strain error. The other formulations  
493 with the traditional constraint ratio show lower accuracy and error convergence  
494 rates.

495 Furthermore, the influence of the integration scheme for this problem is  
496 investigated. As shown in Tables 4 and 5, the integration order  $n_o$  is varied  
497 from 1 to 5 for triangular elements and from 1 to 11 for quadrilateral elements.  
498 The results show that the proposed mixed formulations are not sensitive to the  
499 integration order. Using the traditional lower-order Gauss integration scheme  
500 can sufficiently obtain accurate results. This is consistent with the previous  
analysis in Section 4.1.

Table 4: Error comparison with different triangular integration schemes for plate with hole problem

$n_o$	$n_g$ for $\Omega$	$n_g$ for $\Gamma$	Tri3-RK		Tri6-RK	
			$\ \mathbf{u} - \mathbf{u}_h\ _V$	$\ p - p_h\ _Q$	$\ \mathbf{u} - \mathbf{u}_h\ _V$	$\ p - p_h\ _Q$
1	1	1	3.11E-2	3.53E-3	8.53E17	1.31E4
2	3	2	3.11E-2	3.67E-3	8.33E-3	1.20E-3
3	4	2	3.11E-2	3.67E-3	8.32E-3	1.20E-3
4	6	3	3.11E-2	3.68E-3	8.32E-3	1.22E-3
5	7	3	3.11E-2	3.68E-3	8.32E-3	1.22E-3

$n_o$ : Integration order  $n_g$ : Number of integration points

501

Table 5: Error comparison with different quadrilateral integration schemes for plate with hole problem

$n_o$	$n_g$ for $\Omega$	$n_g$ for $\Gamma$	Quad4-RK		Quad8-RK	
			$\ \mathbf{u} - \mathbf{u}_h\ _V$	$\ p - p_h\ _Q$	$\ \mathbf{u} - \mathbf{u}_h\ _V$	$\ p - p_h\ _Q$
1	3	1	3.64E-2	5.01E-3	9.53E13	8.15E-1
3	$2 \times 2$	2	3.64E-2	5.09E-3	4.33E-2	8.84E-3
5	$3 \times 3$	3	3.62E-2	3.71E-3	1.27E-3	4.42E-5
7	$4 \times 4$	4	3.62E-2	3.70E-3	1.26E-3	1.49E-4
9	$5 \times 5$	5	3.62E-2	3.70E-3	1.26E-3	1.50E-4
11	$6 \times 6$	6	3.62E-2	3.70E-3	1.26E-3	1.50E-4

$n_o$ : Integration Order  $n_g$ : Number of integration points

### 502 5.3. Cook's membrane problem

503 The Cook's membrane problem [12] is used herein for stability analysis of  
504 pressure. The geometry of this problem is shown in Figure 23, in which the left

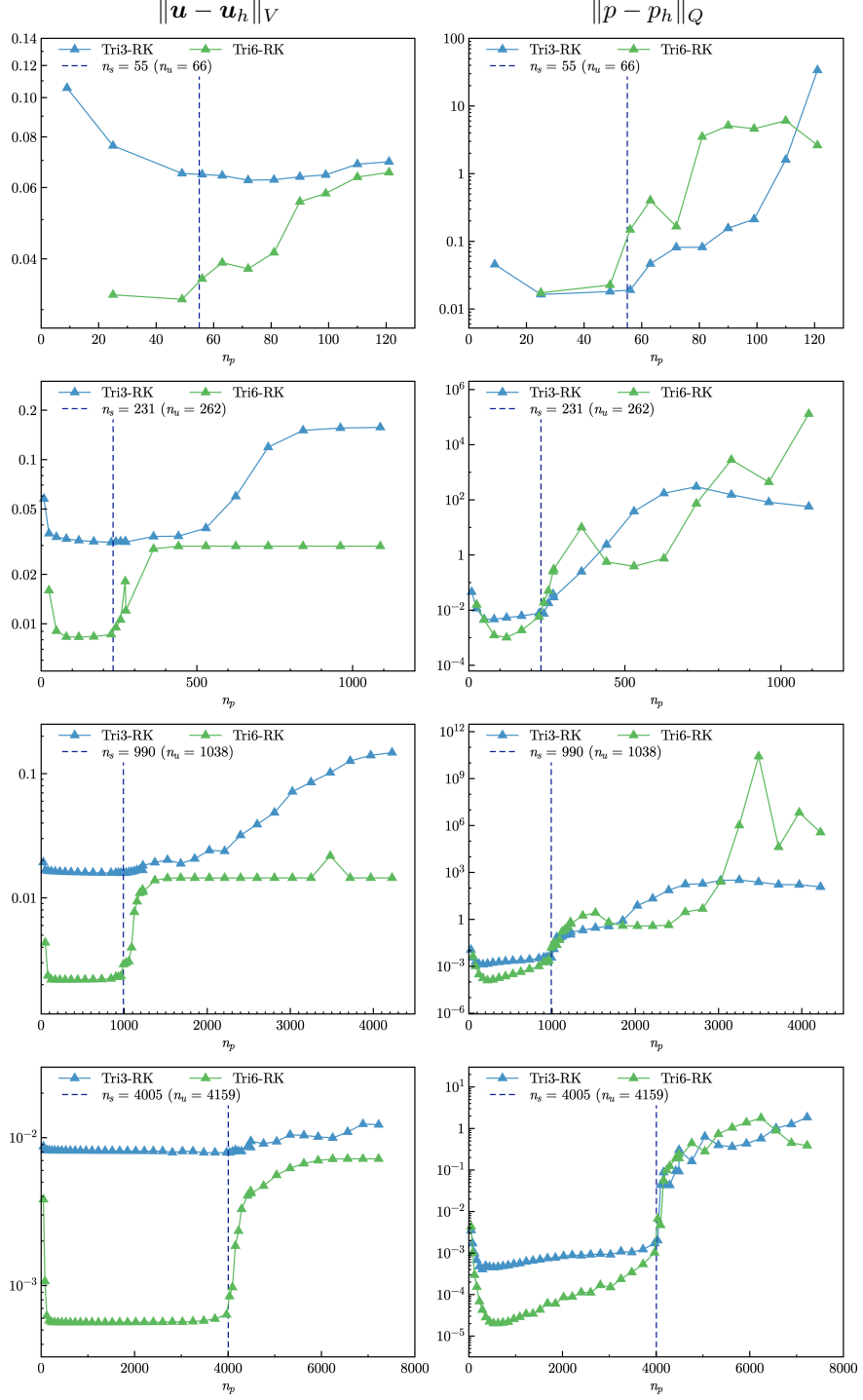


Figure 19: Strain and pressure errors vs.  $n_p$  for plate with hole problem with triangular elements

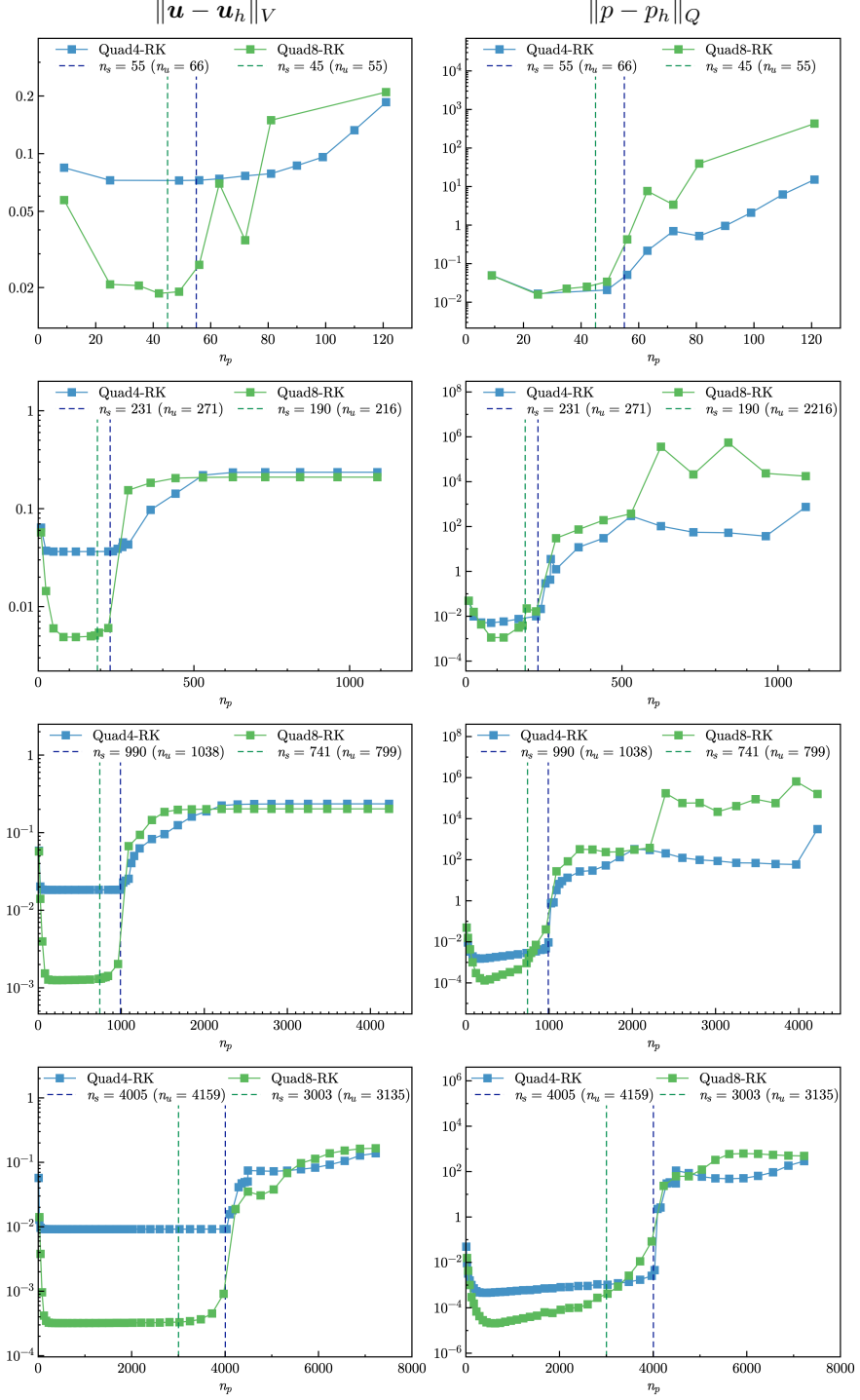


Figure 20: Strain and pressure errors vs.  $n_p$  for plate with hole problem with quadrilateral elements

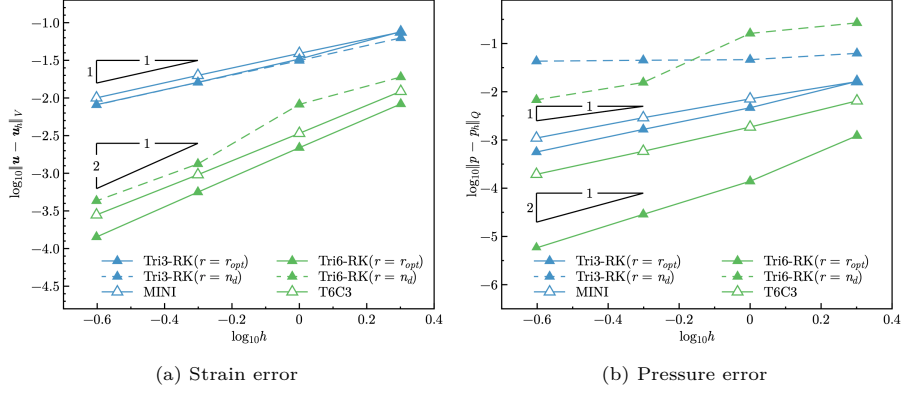


Figure 21: Error convergence study for plate with hole problem with triangular elements

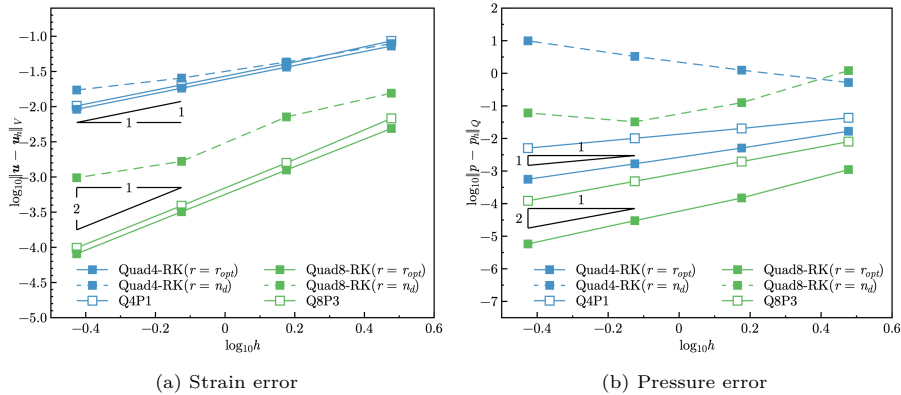


Figure 22: Error convergence study for plate with hole problem with quadrilateral elements

505 hand side is fixed and the right hand side subjects a concentrated force  $P = 6.25$   
 506 in the  $y$ -direction. The material parameters are Young's modulus  $E = 70.0$  and  
 507 Poisson's ratio  $\nu = 0.5 - 10^{-8}$ .

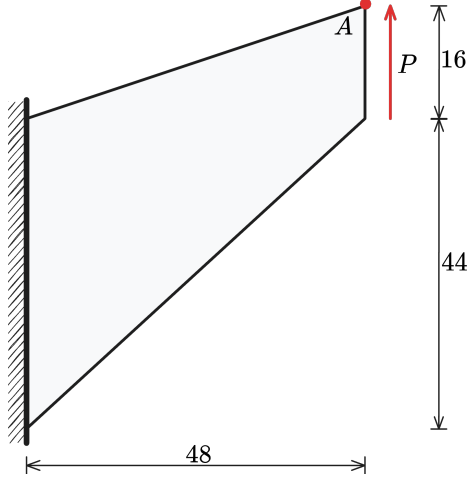


Figure 23: Illustration of Cook's membrane problem

508 In this test, we evaluated the convergence properties by comparing the ver-  
 509 tical displacement at point  $A$  against a reference value of 28.0. As shown in  
 510 Figure 24 illustrates, the methods employing  $r = r_{opt}$  produced results that  
 511 were notably closer to this reference value than those using  $r = n_d$ . Further-  
 512 more, to investigate stability, Figures 25–28 show the pressure contour plots for  
 513 non-uniform Tri3–RK, Tri6–RK, Quad4–RK, and Quad8–RK formulations with  
 514  $r = n_d$  and  $r = r_{opt}$ , respectively. The reproducing kernel meshfree approxima-  
 515 tions are employed for pressure discretization with characterized support sizes  
 516 of 1.5 for the linear basis function and 2.5 for the quadratic basis function. The  
 517 results imply that the pressure contour plots with the optimal constraint ratio  
 518  $r = r_{opt}$  show a more stable and smooth pressure distribution compared to those  
 519 with the traditional constraint ratio  $r = n_d$ .

520 An efficiency comparison of different methods for the Cook's membrane  
 521 problem is presented in Table 6. This includes the condition number of the  
 522 global stiffness matrix and the CPU time for shape function construction, sys-  
 523 tem assembly, and system solving. The mixed FE–Meshfree formulations exhibit  
 524 higher condition number spend more time compared to the traditional element-  
 525 based formulations. This is mainly due to the implicit, complicated expression  
 526 of meshfree shape functions and the larger bandwidth of the stiffness matrix,  
 527 which results from the larger support size of the meshfree shape functions.

#### 528 5.4. Block under compression problem

529 The incompressible block problem [62] shown in Figure 29 is considered for  
 530 testing 3D mixed formulations. The block's dimensions are  $2L \times 2L \times L$ ,  $L = 1$ .

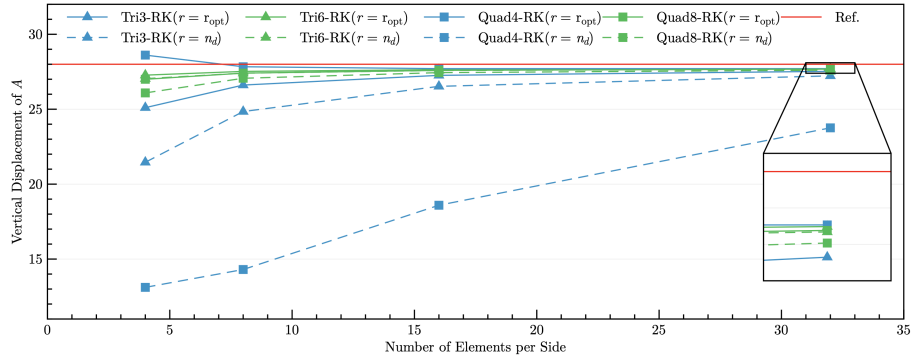


Figure 24: Convergence comparison of the vertical displacement at point  $A$  for Cook's membrane problem

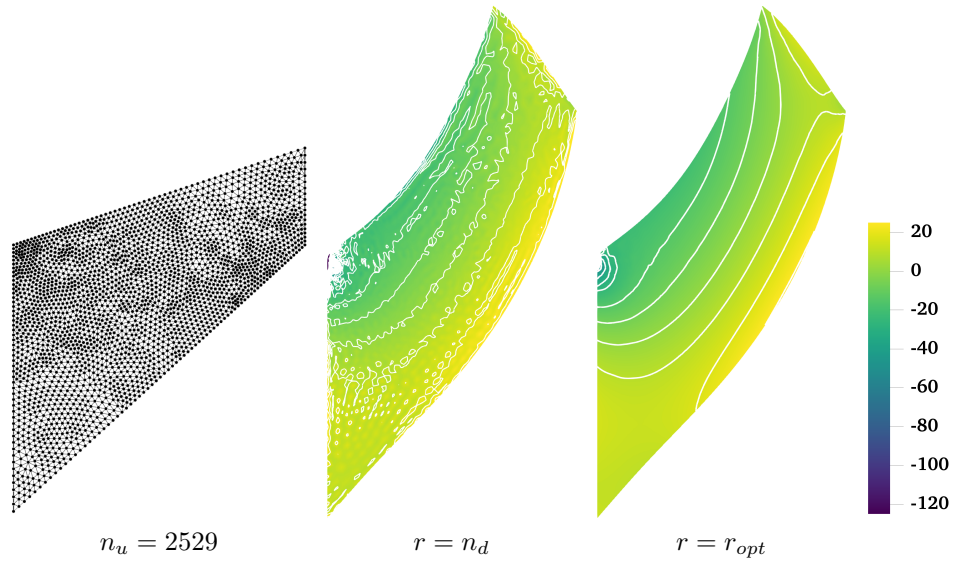


Figure 25: Pressure contour plots for Cook's membrane problem using Tri3-RK

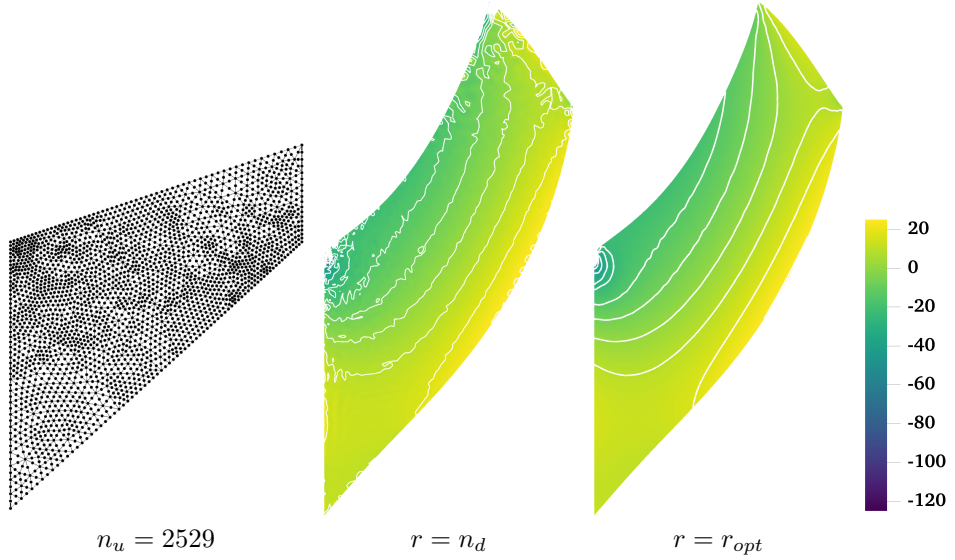


Figure 26: Comparison of pressure contour plots for Cook's membrane problem using Tri6–RK

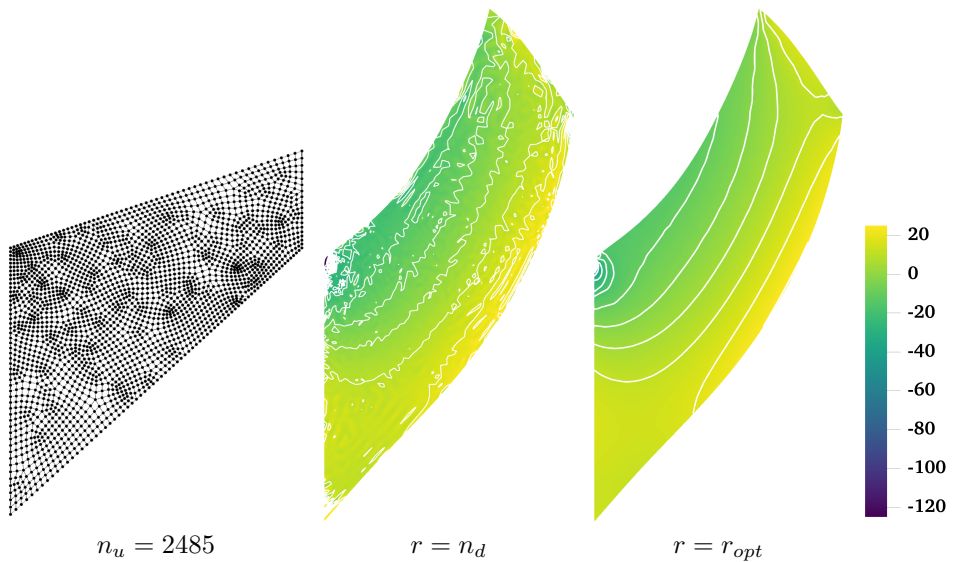


Figure 27: Comparison of pressure contour plots for Cook's membrane problem using Quad4–RK

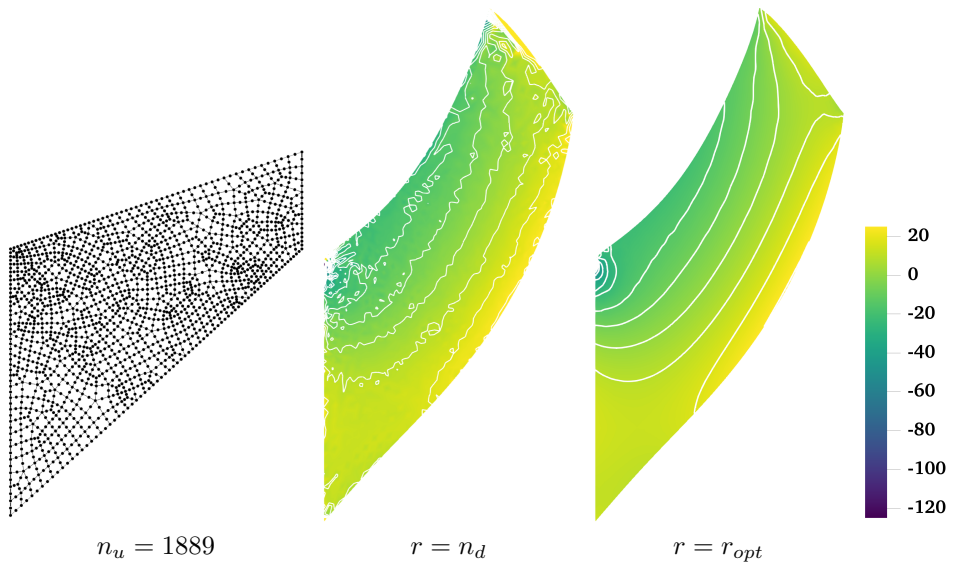


Figure 28: Comparison of pressure contour plots for Cook’s membrane problem using Quad8–RK

Table 6: Condition number and efficiency comparison for Cook’s membrane problem

Method	Condition number	CPU-time (s) for			Solving
		Shape function	Assembly		
MINI	1.11E06	0.025	0.327	0.022	
Tri3–RK( $r = n_d$ )	1.89E10	1.730	4.160	0.108	
Tri3–RK( $r = r_{opt}$ )	1.13E08	1.290	1.720	0.052	
T6C3	1.62E05	0.004	0.380	0.021	
Tri6–RK( $r = n_d$ )	2.48E16	1.620	1.670	0.294	
Tri6–RK( $r = r_{opt}$ )	3.69E10	1.110	0.634	0.077	
Q4P1	5.75E12	0.011	0.344	0.021	
Quad4–RK( $r = n_d$ )	5.21E10	2.100	4.890	0.122	
Quad4–RK( $r = r_{opt}$ )	1.97E08	1.500	2.140	0.057	
Q8P3	2.69E07	0.005	0.373	0.015	
Quad8–RK( $r = n_d$ )	2.75E15	1.170	1.180	0.184	
Quad8–RK( $r = r_{opt}$ )	8.67E10	0.847	0.471	0.065	

531 At the center of the top surface of the block is applied a pressure load  $P$  with  
 532 the area of  $L \times L$ . Due to the symmetry of this problem, only a quarter model is  
 533 considered. The Young's modulus and Poisson's ratio are set as  $E = 240.56839$   
 534 and  $\nu = 0.5 - 10^{-8}$ , respectively.

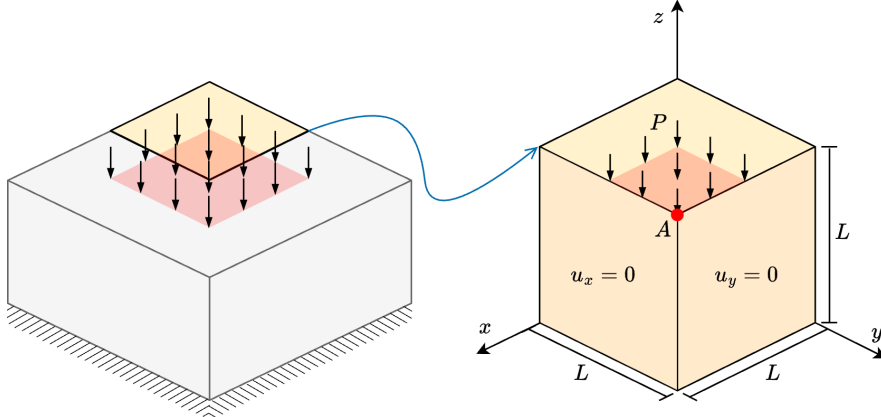


Figure 29: Illustration of block under compression problem

535 The convergence properties of the mixed formulations are evaluated by com-  
 536 paring the compression level at point  $A$  under loading condition  $P = 80$ . The  
 537 4-node tetrahedron element with the MINI scheme (Tet4-MINI) and the 8-node  
 538 hexahedron element with piecewise constant pressure formulation (H8P1) are  
 539 introduced herein as comparison methods. As shown in Figure 30, all the results  
 540 exhibit good convergence behavior across different loading levels. Figures 31, 32  
 541 study the pressure stability of 3D mixed FE-meshfree formulations, Tet4-RK  
 542 and Hex8-RK, with non-uniform nodal distribution, while the pressure is dis-  
 543 cretized by linear meshfree approximations with a characterized support size of  
 544 1.5. The corresponding results also show the well performance of the proposed  
 545 optimal constraint ratio  $r = r_{opt}$ . The mixed formulations with the traditional  
 546 constraint ratio  $r = n_d$  show comparable displacement results, but exhibit sig-  
 547 nificant pressure instability.

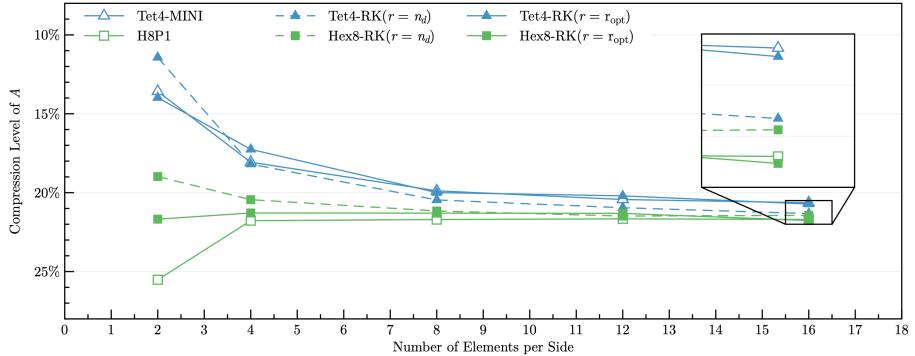


Figure 30: Convergence comparison of compression level (%) at point  $A$  for block under compression problem

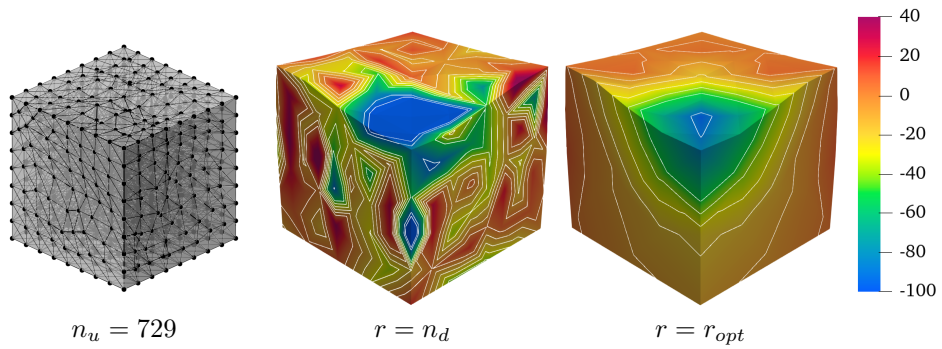


Figure 31: Comparison of pressure contour plots for block under compression problem using Tet4-RK

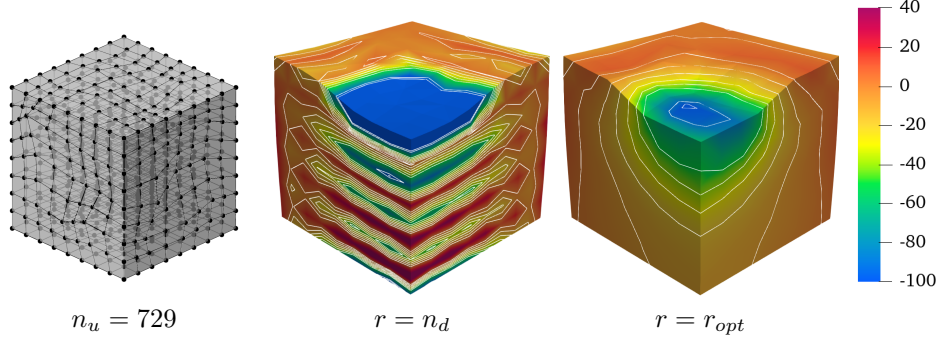


Figure 32: Comparison of pressure contour plots for block under compression problem using Hex8-RK

548    **6. Conclusion**

549    This paper proposes a novel optimal constraint ratio derived from the inf-sup  
550    condition to address volumetric locking. The optimal constraint ratio requires  
551    that, for a given number of displacement DOFs, the number of pressure DOFs  
552    should remain below a stabilized number determined by the proposed inf-sup  
553    value estimator. For a well-posed nodal distribution, simply counting the dis-  
554    placement and pressure DOFs can determine whether the formulation satisfies  
555    the inf-sup condition. Compared to the traditional constraint ratio, the pro-  
556    posed ratio is theoretically grounded in the inf-sup condition and thus is more  
557    precise, and it also provides a simple way, by counting the DOFs of displacement  
558    and pressure fields, to justify the satsification of inf-sup condtiion.

559    To implement this constraint ratio, a mixed finite element (FE) and meshfree  
560    formulation is developed. Displacements are discretized using 3-node and 6-  
561    node triangular elements, 4-node and 8-node quadrilateral elements in 2D, and  
562    4-node tetrahedral and 8-node hexahedral elements in 3D. Correspondingly,  
563    linear and quadratic reproducing kernel meshfree approximations are used for  
564    pressure discretization. The reproducing kernel approximation equips globally  
565    smooth shape functions, allowing arbitrary pressure DOF placement without  
566    the limit of element. However, the implicit expression of shape functions and  
567    the larger bandwidth of the stiffness matrix in meshfree approximation also lead  
568    to larger condition number and lower efficiency compared with traditional FE  
569    formulations.

570    Inf-sup tests for mixed FE-meshfree formulations with different constraint  
571    ratios verify the effectiveness of the proposed inf-sup value estimator. For effi-  
572    ciency and ease of implementation, the final nodal distribution scheme selects  
573    every other displacement node as a pressure node, ensuring the optimal con-  
574    straint ratio and satisfying the inf-sup condition.

575    A series of 2D and 3D incompressible elasticity examples demonstrate the  
576    effectiveness of the proposed mixed formulation. Results show that formulations  
577    with the optimal constraint ratio yield accurate displacement and pressure solu-  
578    tions. When the constraint ratio exceeds the optimal value, errors rise sharply  
579    to unacceptable levels, with the 8-node quadrilateral element being the only  
580    exception that maintains good displacement accuracy. Error convergence stud-  
581    ies and pressure contour plots further confirm that mixed formulations with  
582    the optimal constraint ratio achieve optimal convergence rates and effectively  
583    suppress pressure oscillations.

584    **Acknowledgment**

585    The support of this work by the National Natural Science Foundation of  
586    China (12102138), the Natural Science Foundation of Fujian Province of China  
587    (2023J01108) and the Fundamental Research Funds of Central Universities  
588    (ZQN-1014) is gratefully acknowledged.

589      **References**

- 590      [1] F. Brezzi, M. Fortin, Mixed and Hybrid Finite Element Methods, Vol. 15 of  
591           Springer Series in Computational Mathematics, Springer, New York, NY,  
592           1991.
- 593      [2] T. J. Hughes, The Finite Element Method: Linear Static and Dynamic  
594           Finite Element Analysis, Prentice Hall, New Jersey, 2000.
- 595      [3] I. Babuška, R. Narasimhan, The Babuška-Brezzi condition and the patch  
596           test: An example, Computer Methods in Applied Mechanics and Engineering 140 (1-2) (1997) 183–199.
- 598      [4] K. J. Bathe, Finite Element Procedures, Prentice Hall, Englewood Cliffs,  
599           New Jersey, 1996.
- 600      [5] D. S. Malkus, Eigenproblems associated with the discrete LBB condition for  
601           incompressible finite elements, International Journal of Engineering Science  
602           19 (10) (1981) 1299–1310.
- 603      [6] D. Chapelle, K. J. Bathe, The inf-sup test, Computers & Structures 47 (4)  
604           (1993) 537–545.
- 605      [7] F. Brezzi, K. J. Bathe, Studies of finite element procedures the inf-sup  
606           condition equivalent forms and applications.
- 607      [8] D. Gallistl, Rayleigh-Ritz approximation of the inf-sup constant for the  
608           divergence, Mathematics of Computation 88 (315) (2019) 73–89.
- 609      [9] P. Hood, C. Taylor, Navier-Stokes equations using mixed interpolation,  
610           Finite element methods in flow problems (1974) 121–132.
- 611      [10] D. S. Malkus, T. J. Hughes, Mixed finite element methods - Reduced and  
612           selective integration techniques: A unification of concepts, Computer Meth-  
613           ods in Applied Mechanics and Engineering 15 (1) (1978) 63–81.
- 614      [11] T. Shilt, R. Deshmukh, J. J. McNamara, P. J. O'Hara, Solution of nearly  
615           incompressible field problems using a generalized finite element approach,  
616           Computer Methods in Applied Mechanics and Engineering 368 (2020)  
617           113165.
- 618      [12] J. C. Simo, M. S. Rifai, A class of mixed assumed strain methods and  
619           the method of incompatible modes, International Journal for Numerical  
620           Methods in Engineering 29 (8) (1990) 1595–1638.
- 621      [13] M. Broccardo, M. Micheloni, P. Krysl, Assumed-deformation gradient finite  
622           elements with nodal integration for nearly incompressible large deformation  
623           analysis, International Journal for Numerical Methods in Engineering 78 (9)  
624           (2009) 1113–1134.

- 625 [14] W. M. Coombs, T. J. Charlton, M. Cortis, C. E. Augarde, Overcoming volumetric locking in material point methods, Computer Methods in Applied Mechanics and Engineering 333 (2018) 1–21.
- 626
- 627
- 628 [15] S. Saloustros, M. Cervera, S. Kim, M. Chiumenti, Accurate and locking-free analysis of beams, plates and shells using solid elements, Computational Mechanics 67 (2021) 883–914.
- 629
- 630
- 631 [16] J. Simo, R. Taylor, K. Pister, Variational and projection methods for the volume constraint in finite deformation elasto-plasticity, Computer Methods in Applied Mechanics and Engineering 51 (1-3) (1985) 177–208.
- 632
- 633
- 634 [17] C. R. Dohrmann, P. B. Bochev, A stabilized finite element method for the Stokes problem based on polynomial pressure projections, International Journal for Numerical Methods in Fluids 46 (2) (2004) 183–201.
- 635
- 636
- 637 [18] A. Valverde-González, J. Reinoso, B. Dortdivanlioglu, M. Paggi, Locking treatment of penalty-based gradient-enhanced damage formulation for failure of compressible and nearly incompressible hyperelastic materials, Computational Mechanics 72 (2023) 635–662.
- 638
- 639
- 640
- 641 [19] B.-B. Xu, F. Peng, P. Wriggers, Stabilization-free virtual element method for finite strain applications, Computer Methods in Applied Mechanics and Engineering 417 (2023) 116555.
- 642
- 643
- 644 [20] F. S. Liguori, A. Madeo, S. Marfia, G. Garcea, E. Sacco, A stabilization-free hybrid virtual element formulation for the accurate analysis of 2D elasto-plastic problems, Computer Methods in Applied Mechanics and Engineering 431 (2024) 117281.
- 645
- 646
- 647
- 648 [21] R. Alves de Sousa, R. Natal Jorge, R. Fontes Valente, J. César de Sá, A new volumetric and shear locking-free 3D enhanced strain element, Engineering Computations 20 (7) (2003) 896–925.
- 649
- 650
- 651 [22] K.-J. Bathe, The inf–sup condition and its evaluation for mixed finite element methods, Computers & Structures 79 (2) (2001) 243–252.
- 652
- 653 [23] T. J. R. Hughes, Multiscale phenomena: Green’s functions, the Dirichlet-to-Neumann formulation, subgrid scale models, bubbles and the origins of stabilized methods, Computer Methods in Applied Mechanics and Engineering 127 (1) (1995) 387–401.
- 654
- 655
- 656
- 657 [24] R. Rossi, R. Zorrilla, R. Codina, A stabilised displacement-volumetric strain formulation for nearly incompressible and anisotropic materials, Computer Methods in Applied Mechanics and Engineering 377 (2021) 113701.
- 658
- 659
- 660
- 661 [25] E. Karabelas, M. A. F. Gsell, G. Haase, G. Plank, C. M. Augustin, An accurate, robust, and efficient finite element framework with applications to anisotropic, nearly and fully incompressible elasticity, Computer Methods in Applied Mechanics and Engineering 394 (2022) 114887.
- 662
- 663
- 664

- 665 [26] R. Codina, I. Castañar, J. Baiges, Finite element approximation of stabilized mixed models in finite strain hyperelasticity involving displacements and stresses and/or pressure—An overview of alternatives, International Journal for Numerical Methods in Engineering (2024) e7540.
- 666
- 667
- 668
- 669 [27] L. Moreno, R. Wuechner, A. Larese, A mixed stabilized MPM formulation for incompressible hyperelastic materials using Variational Subgrid-Scales, Computer Methods in Applied Mechanics and Engineering 435 (2025) 117621.
- 670
- 671
- 672
- 673 [28] T. J. R. Hughes, L. P. Franca, M. Balestra, A new finite element formulation for computational fluid dynamics: V. Circumventing the babuška-brezzi condition: A stable Petrov-Galerkin formulation of the stokes problem accommodating equal-order interpolations, Computer Methods in Applied Mechanics and Engineering 59 (1) (1986) 85–99.
- 674
- 675
- 676
- 677
- 678 [29] A. N. Brooks, T. J. R. Hughes, Streamline upwind/Petrov-Galerkin formulations for convection dominated flows with particular emphasis on the incompressible Navier-Stokes equations, Computer Methods in Applied Mechanics and Engineering 32 (1) (1982) 199–259.
- 679
- 680
- 681
- 682 [30] L. He, L. Jing, M. Feng, New stabilized mixed finite element methods for two-field poroelasticity with low permeability, Applied Mathematics and Computation 494 (2025) 129285.
- 683
- 684
- 685 [31] D. N. Arnold, F. Brezzi, M. Fortin, A stable finite element for the Stokes equations, CALCOLO 21 (4) (1984) 337–344.
- 686
- 687 [32] F. Auricchio, L. Beirão da Veiga, C. Lovadina, A. Reali, A stability study of some mixed finite elements for large deformation elasticity problems, Computer Methods in Applied Mechanics and Engineering 194 (9-11) (2005) 1075–1092.
- 688
- 689
- 690
- 691 [33] A. Quarteroni, A. Valli, Numerical Approximation of Partial Differential Equations, Springer Series in Computational Mathematics, Springer, Berlin, 1994.
- 692
- 693
- 694 [34] M. Crouzeix, P. Raviart, Conforming and nonconforming finite element methods for solving the stationary Stokes equations I, Revue française d'automatique informatique recherche opérationnelle. Mathématique 7 (R3) (1973) 33–75.
- 695
- 696
- 697
- 698 [35] U. Brink, E. Stein, On some mixed finite element methods for incompressible and nearly incompressible finite elasticity, Computational Mechanics 19 (1) (1996) 105–119.
- 699
- 700
- 701 [36] T. Belytschko, Y. Y. Lu, L. Gu, Element-free Galerkin methods, International Journal for Numerical Methods in Engineering 37 (2) (1994) 229–256.
- 702

- 703 [37] W. K. Liu, S. Jun, Y. F. Zhang, Reproducing kernel particle methods, International Journal for Numerical Methods in Fluids 20 (8-9) (1995) 1081–  
 704 1106.
- 706 [38] C. Rodriguez, T.-H. Huang, A variationally consistent reproducing kernel enhanced material point method and its applications to incompressible  
 707 materials, Computational Mechanics (2023) 1–20.
- 709 [39] S. W. Chi, J. S. Chen, H. Y. Hu, A weighted collocation on the strong form with mixed radial basis approximations for incompressible linear elasticity,  
 710 Computational Mechanics 53 (2) (2014) 309–324.
- 712 [40] L. Wang, Z. Qian, Y. Zhou, Y. Peng, A weighted meshfree collocation method for incompressible flows using radial basis functions, Journal of  
 713 Computational Physics 401 (2020) 108964.
- 715 [41] A. Ortiz-Bernardin, M. Puso, N. Sukumar, Improved robustness for nearly-incompressible large deformation meshfree simulations on Delaunay tessellations, Computer Methods in Applied Mechanics and Engineering 293 (2015) 348–374.
- 719 [42] T. J. Hughes, J. A. Cottrell, Y. Bazilevs, Isogeometric analysis: CAD, finite elements, NURBS, exact geometry and mesh refinement, Computer Methods in Applied Mechanics and Engineering 194 (39-41) (2005) 4135–  
 720 4195.
- 723 [43] F. Auricchio, L. Beirão da Veiga, C. Lovadina, A. Reali, The importance of the exact satisfaction of the incompressibility constraint in nonlinear elasticity: Mixed FEMs versus NURBS-based approximations, Computer Methods in Applied Mechanics and Engineering 199 (5) (2010) 314–323.
- 727 [44] A. Huerta, S. Fernández-Méndez, Locking in the incompressible limit for the element-free Galerkin method, International Journal for Numerical Methods in Engineering 51 (11) (2001) 1361–1383.
- 730 [45] J. Dolbow, T. Belytschko, Volumetric locking in the element free Galerkin method, International Journal for Numerical Methods in Engineering 46 (6) (1999) 925–942.
- 733 [46] G. Moutsanidis, J. J. Koester, M. R. Tupek, J.-S. Chen, Y. Bazilevs, Treatment of near-incompressibility in meshfree and immersed-particle methods, Computational Particle Mechanics 7 (2) (2020) 309–327.
- 736 [47] G. Moutsanidis, W. Li, Y. Bazilevs, Reduced quadrature for FEM, IGA and meshfree methods, Computer Methods in Applied Mechanics and Engineering 373 (2021) 113521.
- 739 [48] Z.-Y. Wang, Y.-F. Jin, Z.-Y. Yin, Y.-Z. Wang, Overcoming volumetric locking in stable node-based smoothed particle finite element method with cubic bubble function and selective integration, International Journal for Numerical Methods in Engineering 123 (24) (2022) 6148–6169.

- 743 [49] T. Elguedj, Y. Bazilevs, V. Calo, T. Hughes, B<sup>−</sup> and F<sup>−</sup> projection methods  
 744 for nearly incompressible linear and non-linear elasticity and plasticity  
 745 using higher-order NURBS elements, Computer Methods in Applied Mechanics and Engineering 197 (33-40) (2008) 2732–2762.
- 746
- 747 [50] J. S. Chen, S. Yoon, H. P. Wang, W. K. Liu, An improved reproducing  
 748 kernel particle method for nearly incompressible finite elasticity, Computer  
 749 Methods in Applied Mechanics and Engineering 181 (1) (2000) 117–145.
- 750
- 751 [51] C. M. Goh, P. M. F. Nielsen, M. P. Nash, A stabilised mixed mesh-  
 752 free method for incompressible media: Application to linear elasticity and  
 753 Stokes flow, Computer Methods in Applied Mechanics and Engineering 329  
 754 (2018) 575–598.
- 755
- 756 [52] D. S. Bombarde, M. Agrawal, S. S. Gautam, A. Nandy, Hellinger–Reissner  
 757 principle based stress–displacement formulation for three-dimensional iso-  
 758 geometric analysis in linear elasticity, Computer Methods in Applied Mechanics and Engineering 394 (2022) 114920.
- 759
- 760 [53] H. Casquero, M. Golestanian, Vanquishing volumetric locking in quadratic  
 761 NURBS-based discretizations of nearly-incompressible linear elasticity:  
 762 CAS elements, Computational Mechanics 73 (6) (2024) 1241–1252.
- 763
- 764 [54] A. Huerta, Y. Vidal, P. Villon, Pseudo-divergence-free element free  
 765 Galerkin method for incompressible fluid flow, Computer Methods in Applied  
 766 Mechanics and Engineering 193 (12-14) (2004) 1119–1136.
- 767
- 768 [55] C. T. Wu, W. Hu, J. S. Chen, A meshfree-enriched finite element method  
 769 for compressible and near-incompressible elasticity, International Journal  
 770 for Numerical Methods in Engineering 90 (7) (2012) 882–914.
- 771
- 772 [56] T. Vu-Huu, C. Le-Thanh, H. Nguyen-Xuan, M. Abdel-Wahab, A high-  
 773 order mixed polygonal finite element for incompressible Stokes flow analy-  
 774 sis, Computer Methods in Applied Mechanics and Engineering 356 (2019)  
 775 175–198.
- 776
- 777 [57] E. Stein, R. de Borst, T. J. R. Hughes (Eds.), Encyclopedia of Computa-  
 778 tional Mechanics, John Wiley, Chichester, West Sussex, 2004.
- 779
- 780 [58] I. Babuška, J. Osborn, Eigenvalue Problems, in: Handbook of Numerical  
 781 Analysis, Vol. 2 of Finite Element Methods (Part 1), Elsevier, 1991, pp.  
 782 641–787.
- 783
- 784 [59] K. Yosida, Functional Analysis, 6th Edition, Classics in Mathematics,  
 785 Springer-Verlag, Berlin Heidelberg, 1995.
- 786
- 787 [60] J. Wu, D. Wang, An accuracy analysis of Galerkin meshfree methods ac-  
 788 counting for numerical integration, Computer Methods in Applied Mechan-  
 789 ics and Engineering 375 (2021) 113631.
- 790

- <sup>781</sup> [61] S. Timoshenko, J. Goodier, Theory of Elasticity, Engineering Mechanics  
<sup>782</sup> Series, McGraw-Hill, 1969.
- <sup>783</sup> [62] S. Reese, P. Wriggers, B. D. Reddy, A new locking-free brick element tech-  
<sup>784</sup> nique for large deformation problems in elasticity, Computers & Structures  
<sup>785</sup> 75 (3) (2000) 291–304.
- <sup>786</sup> [63] S. C. Brenner, L. R. Scott, The Mathematical Theory of Finite Element  
<sup>787</sup> Methods, Springer, New York, 2008.

788     **Appendix A. Error estimator for mixed-formulation**

789     In this appendix, the traditional error estimators for mixed-formulation are  
 790     illustrated herein, the proof is referred to [63]. For incompressible elasticity  
 791     problems, i.e.  $\kappa \rightarrow \infty$ ,  $c(q, p) = 0$ , the weak formula of Eq. (14) is rewritten as:  
 792     Find  $\mathbf{u}_h \in V_h, p_h \in Q_h$ ,

$$\begin{aligned} a(\mathbf{v}_h, \mathbf{u}_h) + b(\mathbf{v}_h, p_h) &= f(\mathbf{v}_h), & \forall \mathbf{v}_h \in V_h \\ b(\mathbf{u}_h, q_h) &= 0, & \forall q_h \in Q_h \end{aligned} \quad (\text{A.1})$$

793     According to the definition of bilinear form  $b$  in Eq. (10), for a  $\mathbf{u}_h \in \ker \mathcal{P}_h$ , then  
 794     the second equation of Eq. (A.1) is naturally satisfied. Thus, the above weak  
 795     formulation can be equivalently split into the following two steps: Firstly, find  
 796      $\mathbf{u}_h \in \ker \mathcal{P}_h$ ,

$$a(\mathbf{v}_h, \mathbf{u}_h) = f(\mathbf{v}_h), \quad \forall \mathbf{v}_h \in \ker \mathcal{P}_h \quad (\text{A.2})$$

797     After determine  $\mathbf{u}_h$ , then find  $p_h \in Q_h$ ,

$$b(\mathbf{v}_h, p_h) = f(\mathbf{v}_h) - a(\mathbf{v}_h, \mathbf{u}_h), \quad \forall \mathbf{v}_h \in V_h \quad (\text{A.3})$$

798     To further analyze the error of mixed-formulation, the following properties  
 799     of bilinear forms  $a$  and  $b$  should be defined [63]:

800     • **Continuity:**

$$a(\mathbf{v}, \mathbf{u}) \leq C_a \|\mathbf{v}\|_V \|\mathbf{u}\|_V, \quad \forall \mathbf{v}, \mathbf{u} \in V \quad (\text{A.4})$$

$$b(\mathbf{v}, q) \leq C_b \|\mathbf{v}\|_V \|q\|_Q, \quad \forall \mathbf{v} \in V, \forall q \in Q \quad (\text{A.5})$$

801     • **Coercivity:**

$$\|\mathbf{v}\|_V \leq \frac{1}{\alpha} \sup_{\mathbf{w} \in V} \frac{|a(\mathbf{v}, \mathbf{w})|}{\|\mathbf{w}\|_V}, \quad \forall \mathbf{v} \in V \quad (\text{A.6})$$

802     • **Inf-sup condition:**

$$\|q\|_Q \leq \frac{1}{\beta} \sup_{\mathbf{v} \in V} \frac{|b(\mathbf{v}, q)|}{\|\mathbf{v}\|_V}, \quad \forall q \in Q \quad (\text{A.7})$$

803     where  $C_a$  and  $C_b$  are positive constants independent of mesh size  $h$ .  $\alpha$  and  $\beta$   
 804     are the coercivity and inf-sup constants, respectively, which will influence the  
 805     accuracy of mixed-formulation.

806     For the error of displacement, the Céa's Theorem used for the error analysis  
 807     of traditional Galerkin formulation is not always valid for mixed-formulation.  
 808     This is because most of mixed-formulation can not ensure  $\ker \mathcal{P}_h \subset \ker \mathcal{P}$  to  
 809     maintain the orthogonality of bilinear form  $a$  that is required in the proof of  
 810     Céa's Theorem. So we first introduce the following error estimator for displacement  
 811     in the case of  $\ker \mathcal{P}_h \not\subset \ker \mathcal{P}$ . For any  $\mathbf{v}_h \in \ker \mathcal{P}_h$ , considering the triangle

<sup>812</sup> inequality, the coercivity in Eq. (A.6) and the continuity in Eq. (A.4), we have:

$$\begin{aligned}
\|\mathbf{u} - \mathbf{u}_h\|_V &\leq \|\mathbf{u} - \mathbf{v}_h\|_V + \|\mathbf{v}_h - \mathbf{u}_h\|_V \\
&\leq \|\mathbf{u} - \mathbf{v}_h\|_V + \frac{1}{\alpha} \sup_{\mathbf{w}_h \in \ker \mathcal{P}_h} \frac{|a(\mathbf{v}_h - \mathbf{u}_h, \mathbf{w}_h)|}{\|\mathbf{w}_h\|_V} \\
&\leq \|\mathbf{u} - \mathbf{v}_h\|_V + \frac{1}{\alpha} \sup_{\mathbf{w}_h \in \ker \mathcal{P}_h} \frac{|a(\mathbf{v}_h - \mathbf{u}, \mathbf{w}_h)| + |a(\mathbf{u} - \mathbf{u}_h, \mathbf{w}_h)|}{\|\mathbf{w}_h\|_V} \quad (\text{A.8}) \\
&\leq (1 + \frac{C}{\alpha}) \|\mathbf{u} - \mathbf{v}_h\|_V + \frac{1}{\alpha} \sup_{\mathbf{w}_h \in \ker \mathcal{P}_h} \frac{|a(\mathbf{u} - \mathbf{u}_h, \mathbf{w}_h)|}{\|\mathbf{w}_h\|_V}
\end{aligned}$$

<sup>813</sup> According to Eqs. (A.2), (A.3) and continuity in Eq. (A.5), the second term on  
<sup>814</sup> the right hand side of above equation can be rewritten as:

$$\begin{aligned}
\sup_{\mathbf{w}_h \in \ker \mathcal{P}_h} \frac{|a(\mathbf{u} - \mathbf{u}_h, \mathbf{w}_h)|}{\|\mathbf{w}_h\|_V} &= \sup_{\mathbf{w}_h \in \ker \mathcal{P}_h} \frac{|a(\mathbf{u}, \mathbf{w}_h) - f(\mathbf{w}_h)|}{\|\mathbf{w}_h\|_V} \\
&= \sup_{\mathbf{w}_h \in \ker \mathcal{P}_h} \frac{|b(\mathbf{w}_h, p)|}{\|\mathbf{w}_h\|_V} \quad (\text{A.9}) \\
&= \sup_{\mathbf{w}_h \in \ker \mathcal{P}_h} \frac{|b(\mathbf{w}_h, p - q_h)|}{\|\mathbf{w}_h\|_V} \\
&\leq C_b \|p - q_h\|_Q
\end{aligned}$$

<sup>815</sup> where  $q_h$  is an arbitrary variable in  $Q_h$ . Combining the Eqs. (A.8) and (A.9),  
<sup>816</sup> the following error estimator for displacement can be obtained:

$$\|\mathbf{u} - \mathbf{u}_h\|_V \leq (1 + \frac{C_a}{\alpha}) \inf_{\mathbf{v}_h \in \ker \mathcal{P}_h} \|\mathbf{u} - \mathbf{v}_h\|_V + \frac{C_b}{\alpha} \inf_{q_h \in Q_h} \|p - q_h\|_Q \quad (\text{A.10})$$

<sup>817</sup> Furthermore, for the error estimator of pressure, according to the first equa-  
<sup>818</sup> tion of Eq. (6) and  $V_h \subset V$ , we have:

$$b(\mathbf{v}_h, p) = f(\mathbf{v}_h) - a(\mathbf{v}_h, \mathbf{u}), \quad \forall \mathbf{v}_h \in V_h \quad (\text{A.11})$$

<sup>819</sup> and then subtracting Eq. (A.11) from Eq. (A.3) yields:

$$b(\mathbf{v}_h, p - p_h) = -a(\mathbf{v}_h, \mathbf{u} - \mathbf{u}_h), \quad \forall \mathbf{v}_h \in V_h \quad (\text{A.12})$$

<sup>820</sup> In this context, for any  $q_h \in Q_h$ , invoking the triangle inequality, Eqs. (A.7)  
<sup>821</sup> and (A.5) leads to:

$$\begin{aligned}
\|p - p_h\|_Q &\leq \|p - q_h\|_Q + \|q_h - p_h\|_Q \\
&\leq \|p - q_h\|_Q + \frac{1}{\beta} \sup_{\mathbf{v} \in V_h} \frac{|b(\mathbf{v}_h, q_h - p_h)|}{\|\mathbf{v}_h\|_V} \\
&\leq \|p - q_h\|_Q + \frac{1}{\beta} \sup_{\mathbf{v} \in V_h} \frac{|a(\mathbf{v}_h, \mathbf{u} - \mathbf{u}_h)| + |b(\mathbf{v}_h, p - q_h)|}{\|\mathbf{v}_h\|_V} \quad (\text{A.13}) \\
&\leq \frac{C_a}{\beta} \|\mathbf{u} - \mathbf{u}_h\|_V + (1 + \frac{C_b}{\beta}) \|p - q_h\|_Q
\end{aligned}$$

822 Consequently, the error estimator for pressure can be given by:

$$\|p - p_h\|_Q \leq \frac{C_a}{\beta} \|\mathbf{u} - \mathbf{u}_h\|_V + \left(1 + \frac{C_b}{\beta}\right) \inf_{q_h \in Q_h} \|p - q_h\|_Q \quad (\text{A.14})$$

823 Obviously, the error estimators of Eqs. (A.10) and (A.14) are both related  
 824 to the coercivity constant  $\alpha$ , inf-sup constant  $\beta$  and the approximability of  
 825 spaces  $\ker \mathcal{P}_h$ ,  $Q_h$ , in which the approximability is usually measured by the  
 826 interpolation error of approximation method. However, the approximability  
 827 of space  $\ker \mathcal{P}_h$  is not trivial to be evaluated directly. To further evaluate the  
 828 approximability of space  $\ker \mathcal{P}_h$ , let a variable  $\mathbf{w}_h \in V_h \setminus \ker \mathcal{P}_h$  to satisfy the  
 829 following relationship:

$$\inf_{\bar{\mathbf{v}}_h \in \ker \mathcal{P}_h} \|\mathbf{u} - (\bar{\mathbf{v}}_h + \mathbf{w}_h)\|_V = \inf_{\mathbf{v}_h \in V_h} \|\mathbf{u} - \mathbf{v}_h\|_V \quad (\text{A.15})$$

830 such that the approximability of space  $\ker \mathcal{P}_h$  can be transformed to that of  
 831 space  $V_h$  that is easy to be measured. If  $\mathbf{w}_h = \mathbf{0}$ ,  $\ker \mathcal{P}_h$  has the identical  
 832 approximability with  $V_h$ :

$$\inf_{\bar{\mathbf{v}}_h \in \ker \mathcal{P}_h} \|\mathbf{u} - \bar{\mathbf{v}}_h\|_V = \inf_{\mathbf{v}_h \in V_h} \|\mathbf{u} - \mathbf{v}_h\|_V \quad (\text{A.16})$$

833 If  $\mathbf{w}_h \neq \mathbf{0}$ , leading a triangle inequality we have:

$$\|\mathbf{u} - \bar{\mathbf{v}}_h\|_V \leq \|\mathbf{u} - (\bar{\mathbf{v}}_h + \mathbf{w}_h)\|_V + \|\mathbf{w}_h\|_V \quad (\text{A.17})$$

834 where, reconsidering the Eq. (26) in Lemma 1, as  $\mathbf{w}_h \in V_h \setminus \ker \mathcal{P}_h$  and  $\mathbf{w}_h \neq \mathbf{0}$ ,  
 835 the following relation can be obtained:

$$\|\mathbf{w}_h\|_V \leq \frac{1}{\beta} \|\mathcal{P}_h \mathbf{w}_h\|_Q \quad (\text{A.18})$$

836 where, using Eqs. (25), (17) and considering  $\mathbf{u} \in \ker \mathcal{P}$ ,  $\bar{\mathbf{v}}_h \in \ker \mathcal{P}_h$ , the right  
 837 hand side of above equation can further be transformed as follows:

$$\begin{aligned} \|\mathcal{P}_h \mathbf{w}_h\|_Q &= \sup_{q_h \in Q_h} \frac{|\frac{1}{\kappa}(\mathcal{P}_h \mathbf{w}_h, q_h)|}{\|q_h\|_Q} = \sup_{q_h \in Q_h} \frac{|b(\mathbf{w}_h, q_h)|}{\|q_h\|_Q} \\ &= \sup_{q_h \in Q_h} \frac{|b(\mathbf{u} - (\mathbf{w}_h + \bar{\mathbf{v}}_h), q_h)|}{\|q_h\|_Q} \quad (\text{A.19}) \\ &\leq C_b \|\mathbf{u} - (\mathbf{w}_h + \bar{\mathbf{v}}_h)\|_V \end{aligned}$$

838 With the combination of Eqs. (A.17), (A.18) and (A.19), the approximability  
 839 of  $\ker \mathcal{P}_h$  for the case of  $\mathbf{w}_h \neq \mathbf{0}$  is given by:

$$\inf_{\bar{\mathbf{v}}_h \in \ker \mathcal{P}_h} \|\mathbf{u} - \bar{\mathbf{v}}_h\|_V \leq \left(1 + \frac{C_b}{\beta}\right) \inf_{\mathbf{v}_h \in V_h} \|\mathbf{u} - \mathbf{v}_h\|_V \quad (\text{A.20})$$